Multi-scale analysis of cardiac myoarchitecture

by

Teresa T. Wang

B.S., Materials Science & Engineering (2007)
Massachusetts Institute of Technology

Submitted to the Department of Biological Engineering
in partial fulfillment of the requirements for the degree of

Master of Engineering in Biological Engineering

at the

MASSACHUSETTS INSTITUTE OF TECHNOLOGY

June 2008

Author: _____
Department of Biological Engineering
May 9, 2008

Certified by: _____
Peter So
Professor, Mechanical & Biological Engineering
Thesis Supervisor

Certified by: _____
Richard Gilbert
Research Scientist, Mechanical Engineering
Thesis Supervisor

Accepted by: _____
Alan J. Grodzinsky
Chairman, Department Committee on Graduate Students

Multi-scale analysis of cardiac myoarchitecture

by

Teresa T. Wang

Submitted to the Department of Biological Engineering
on May 9, 2008, in partial fulfillment of the
requirements for the degree of
Masters of Engineering in Biological Engineering

Abstract

The distribution and generation of force within the myocardium during normal contractility is dictated by the tissue's underlying 3D myoarchitecture. The presence of disordered myoarchitecture may in turn constitute the pathological basis of impaired cardiac mechanics in numerous clinical conditions, such as the remodeling heart following myocardial infarction and cardiomyopathies. To investigate the multi-scale nature of architectural disarray in the setting of myocardial disease, a dual imaging approach consisting of diffusion spectrum magnetic resonance imaging (DSI) and high-speed multislice two-photon microscopy (TPM) was used. DSI is a technique that derives fiber orientation from directionality of proton diffusion, whereas TPM derives cellular alignment from an autocorrelation of 3D resolved images of cells and subcellular structure. Mesoscale tract representations of myofiber orientation are generated from similarly aligned diffusion or autocorrelation vectors. These methods were applied to study induced myocardial infarction in the rat and hypertrophic cardiomyopathy associated with deletion of the gene for myosin binding protein C (cMyBP-C) in the mouse. Normal cardiac muscle fiber alignment within the ventricular wall was characterized by a series of helical tracts transitioning from a left-handed orientation in the subepicardium to circumferential in the mid-myocardium to right-handed in the subendocardium. Infarcted hearts displayed a fiber void in the infarct zone and an extension of both subepicardial and subendocardial fibers beyond the border zone. It's hypothesized that the growth of fibers contributes to the remodeling process and provides tensile strength to the myocardium during contraction. The hearts obtained from the cMyBP-C knockouts displayed significant myoarchitectural disarray characterized by a loss of voxel to voxel orientational coherence for fibers located from the mid-myocardium to subendocardium, resulting in a change in the transmural progression of remaining helical fibers. These observations suggest an association between cMyBP-C expression and cardiac fiber alignment, where variations in torsional rotation may constitute a mechanism for pump failure in hypertrophic cardiomyopathy. These results substantiate the use of multi-scale imaging methods to enhance understanding of molecular and cellular contributions to tissue mechanical function.

Thesis Supervisor: Peter So
Title: Professor, Biological and Mechanical Engineering

Thesis Supervisor: Richard Gilbert
Title: Research Scientist: Mechanical Engineering

Acknowledgements

I would like to acknowledge all those who have contributed to the completion of this research. Most importantly, I would like to thank Richard Gilbert, who provided motivation, expertise, and experience throughout this challenging endeavor. I also thank him for opening my eyes to the impact of this research in the world of cardiology and mechanics. I thank Prof. Peter So for his advice on this thesis and providing me an office and desk to work on every day. I thank our collaborators at Massachusetts General Hospital: George Dai, Thomas Benner, Ruopeng Wang, David Sosnovik, and Van Wedeen, for their expertise and endless help. I also thank our collaborators, Srboljub Mijailovich at Harvard Public School of Health, and Dan Fitzsimons and Richard Moss from University of Wisconsin Cardiovascular Research Center, for their knowledge and providing mouse hearts for this project. I thank prior MIT graduate students, Terry Gaige and Sam Felton, for their patience and help with DSI, TrackVis, and TPM autocorrelation. I thank Hyuk-Sang Kwon for acquiring and performing TPM experiments on heart samples. I thank Partha Mondal for sitting at the desk behind me and serving as good company during long days of research; I thank Barry Masters, Jaewon Cha, Heejin Choi, Daekeun Kim, and Yang-Hyo Kim, for their wisdom and random entertaining diversions. I sincerely thank my friends in Boston for keeping me sane this year and encouraging me to follow my instincts and hopes. Lastly, I thank my parents for supporting my choices and everything else.

Contents

List of Figures

Chapter 1

Introduction

1.1 Cardiac structure and function

The heart is a muscular organ with a pumping ability that regulates the rate of blood oxygenation and the delivery of oxygenated blood and nutrients throughout the body. The myocardium, with a total of four chambers, is separated by the septal wall into the right and left half, each composed of an atria and ventricle.

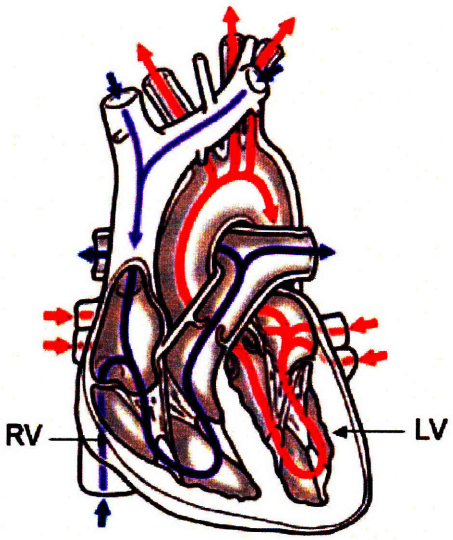

Figure 1.1.1. Circulation of blood through the heart [1]. Deoxygenated blood (blue) flows through the right ventricle (RV) to the lungs. Oxygenated blood (red) flows through the left ventricle (LV) to the body.

From a physiological perspective, the expulsion and uptake of blood from various cardiac chambers can be divided into systole (atrial and ventricular contraction) and diastole (relaxation), respectively [2]. During the course of diastole, blood continues to fill the ventricles until the pressure surpasses that in the pulmonary artery and aorta, at which point the blood is pumped from the right ventricle into the pulmonary artery and from the left ventricle into the aorta. De-oxygenated blood flows from the body thru the right ventricle to the lungs, while oxygenated blood flows from the lungs to the left ventricle into the body (Fig. 1.1.1).

1.2 Cardiac myoarchitecture and mechanics

Cardiac myoarchitecture represents the macroscopic anatomical arrangement of muscle fibers in the myocardium, and is believed to provide a template upon which myocardial contractility occurs. At all stages of maturation, beginning with the embryo, cardiac form and mechanics are associated with one another [3]. The evolution of the heart as a fundamental pumping organ is based on its ability to control mechanics at both the cellular and tissue level. The development of such mechanical forces is reflected in the tissue's 3D fiber orientation.

Streeter et al established that the highly anisotropic fibers of the heart may be portrayed as a series of crossing helical structures, which vary in helix angle as a function of transmural depth and location within the ventricular wall [4]. Through exhaustive histological studies, Streeter et al observed that the fibers in the left ventricular wall varied symmetrically as helices from a left-handed -90° in the subepicardium to a right-handed +90° in the subendocardium [4-6]. On the basis of these observations, Streeter et al modeled the

myocardium as a set of nested fiber shells comprised of helices with gradually changing angles [7]. Each shell consisted of parallel fibers and formed a spiral-like shape around the heart. Others theorized that the myocardium was made of twisted sheets of myocardial cells, each with a thickness of about four cells [8]. The myocytes were tightly bound by collagen within a sheet and loosely bound between sheets to allow shearing and extension of muscle fiber sheets during contractile wall thickening [9]. Torrent-Guasp further modeled the myocardium as a continuous muscular band that twisted upon itself to form two helical loops rather than individual fiber shells [10]. While the details of these theories vary, all depict cardiac fiber structure alignment in a fashion that is considered to be advantageous to mechanical contraction and relaxation.

The myocardium contracts in a torsional manner, exhibiting apical twisting in systole and rapid untwisting in diastole around the long axis [11, 12]. The helical arrangement of fibers is thought to help balance stress and strain throughout the heart during the course of these deformations. Modeled as a "tethered network of muscle fibers", myofiber movement is limited to lateral sliding or shearing, constrained by neighboring myofibers and the myocardial wall [13]. During contraction, the fiber strains shorten in the circumferential and longitudinal directions, but thicken in the radial direction [5]. In normal myocardium, the midwall fibers only stretch circumferentially. Due to the helical orientation of fibers comprising the myocardium, the fibers are theorized to become more longitudinal (non-zero angle) and stretched during contraction [9, 13, 14]. The increase in helix angle of fibers during systole seems to affect fibers in the subendocardium moreso than in the subepicardium [13]. Fibers on the subepicardial surface are more readily able to stretch radially without neighboring cells acting as barriers. Accordingly, the degree of rotation is greater in the

subendocardium than in the subepicardium [12]. In addition, the normal strains felts by the ventricular wall during both systole and diastole are greatest at the subendocardium, even though transmural strains in the fiber direction are uniform.

1.3 Cardiac remodeling following myocardial infarction

Currently, myocardial infarction and its complications are the leading cause of death in the world [15] and can arise from a collection of factors such as genetic predisposition, age, smoking, excessive alcohol consumption, drug abuse, cholesterol levels, diabetes, high blood pressure, obesity, and psychological stress. A myocardial infarction results from an abrupt interruption or obstruction of blood flow to one or several regions of the heart, causing a period of impaired oxygenation (ischemia) or tissue viability. Consequently, the heart takes on a rounder shape as mechanical compensation for the loss of viable muscle tissue in the ischemic zone. The majority of the injured tissue is replaced by scar tissue during the process of remodeling [16]. The ischemic zone is largely characterized by wall thinning, whereas the non-ischemic areas are characterized by hypertrophy and reduced contractility [17, 18]. Infarcted hearts are generally characterized by increases in systolic and diastolic stresses.

Infarcted hearts undergo wound healing driven by the need to sustain normal blood circulation throughout the body. This process of remodeling is largely affected by the loss of cardiomyocyte regeneration and the need to regain mechanical function. Two to three days post infarction, extracellular matrix proteins are deposited on the border zone of the infarction and initiate the formation of granulation tissue [19]. The increase in collagen content in the ischemic area is thought to provide tensile strength and prevent rupture of tissue due to the rhythmic contraction of the non-infarcted cardiac tissue. However, it has also been

shown that collagenolytic activity can also cause distortion to tissue architecture [19]. Surrounding non-infarcted tissue shows signs of myocyte hypertrophy and ventricular dilation to balance the increase in wall stress around the infarct zone [20]. The helicity of normal cardiac myoarchitecture is also disrupted post infarction. In the infarct zone, the percentage of right-handed helices decreased while that of left-handed helices increased; in the remote zones, the opposite trend occurred [21]. In the case of maladaptive remodeling, it is known that the heart fails to fully recover normal mechanical function. Consequently, increase in collagen, myocyte hypertrophy, and fiber disarray can all lead to heart failure [22].

1.4 cMyBP-C gene deletion and hypertrophic cardiomyopathy

One of the largest categories of chronic disease in the world is pump failure related to ischemic, hypertensive, or congenital hypertrophic cardiomyopathy. Inherited diseases like familial hypertrophic cardiomyopathies (FHC) currently afflict up to 1 out of 500 subjects and is the lead cause of cardiac arrest for all age groups [23]. Compared to a normal heart, those afflicted with FHC are characterized by an enlargement of the ventricular walls. This thickening of heart muscle often interferes with normal contraction and relaxation in several ways — narrowing the outflow of blood from the ventricles, reducing the ability of the heart to relax and fill with blood, or by reducing the functionality of the heart valves. Patients often exhibit symptoms including chest pain, dyspnea, and palpitation [23, 24]. The cardiac tissue in FHC patients is often stiff, requiring more pressure for the muscle to contract. FHC is often due to one or more mutations in myofilament proteins, causing contractile dysfunction and pump failure. The myosin binding protein-C (cMyBP-C) is one of the two most common genes that lead to FHC. cMyBP-C is a protein that binds tightly to myosin in thick filaments and acts as a primary regulator of mechanical force and contraction. Because

subjects with FHC are characterized by a decrease in or mutated cMyBP-C expression, homozygous knockout mice were selected to exhibit similar effects.

In normal myocardium, cMyBP-C reversibly binds to phosphate and thereby regulates the interaction and binding between myosin S2 and actin [25, 26]. When unphosphorylated, cMyBP-C binds to myosin, preventing myosin from binding to actin, and vice versa. Upon myosin-actin interaction, thin filaments slide over the thick, creating a change in sarcomere length and inducing contractile movement. It is modeled that cMyBP-C acts to increase the rate of force development at submaximal concentrations of Ca^{2+} [26-29]. The ablation of cMyBP-C acts like permanent phosphorylation, allowing myosin to bind actin more frequently, depending only on the probability of myosin heads coming across actin binding sites. The mechanism between myosin and actin interaction is then affected by changes in the cooperative cross-bridging cycle, namely by increasing the number of strong-binding cross-bridges [28]. Thin filament activation is enhanced by strongly bound cross-bridges, and thereby influences the rate of force development in the myocardium.

cMyBP-C gene deleted mice as young as three weeks displayed signs of hypertrophy through increased measurements of left ventricle to body weight ratios and left ventricular diameters [29, 30]. Histological sections of 14-week-old cMy-BP-$C^{-/-}$ myocardium displayed structural rearrangement of myocytes, which is consistent with pump failure and cardiomyopathy. Previous studies using skinned cardiac myocytes or knockout mice showed increased sensitivity to the Ca^{2+} due to an acceleration of force recovery at lower concentrations of Ca^{2+} [27, 29]. Furthermore, homozygous mice had depressed systolic and diastolic function. More specifically, during systole or contraction, there is a shorter ejection period of blood

flow out of the ventricles. During diastole or relaxation, there is a longer period of time for blood flow into the ventricles. The actual mechanism underlying the development of fiber disorder and hypertrophic cardiomyopathy due to ablation of cMyBP-C remains unknown.

An alternative, and potentially complimentary, mechanism for explaining pump failure in the case of congenital cardiac hypertrophy is the presence of altered myoarchitecture. Such a finding would provide a means for translating cell specific impairments of contractile function to tissue scale deformation and force generation. Impaired myoarchitecture in the absence of cMyBP-C would imply a fundamental link between the expression of proteins regulating rhythmic contraction and those associated with cell adhesion and alignment. Even more compelling, the observation of altered myoarchitecture in the setting of cMyBP-C gene deletion would provide a method for predicting the presence or extent of mechanical dysfunction caused by other named molecular defects.

1.5 Exploration of multi-scale architecture

Diffusion spectrum imaging (DSI) is an imaging method capable of tracking multi-directional molecular diffusion. By deriving the 3D spin displacement function per voxel, DSI is able to determine the alignment of fiber populations [31-33]. From a simple DSI simulation of a set of 2D crossing fiber populations, the calculated orientational distribution function (ODF) mimicked fiber alignment (Fig. 1.5.1) [34].

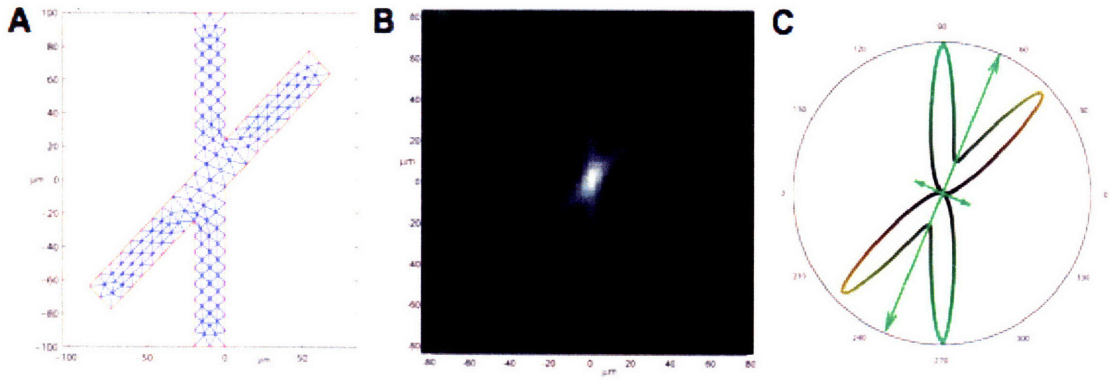

Figure 1.5.1. DSI simulation of 2D crossing fibers [34]. (A) Finite element mesh of crossing muscle fibers. (B) Image depicting average diffusion propagator computed from the mesh. (C) ODF resulting from radial integration of image (B).

This model of water diffusion along a finite element mesh representing crossing muscle fibers resulted in an average diffusion propagator (Fig. 1.5.1B), which was greatest at the center of the crossing fibers. Here, the molecules are most likely to remain around this origin at any given diffusion time. The extensions from the center are aligned with the fiber directions in the mesh. As shown, the ODF is capable of resolving angular relationships of intravoxel crossing fibers and depicting fiber patterns.

Through tractography, fibers derived from microscopic diffusion functions are portrayed at a spatial scale of local deformation in a macroscopic tissue [34, 35]. The reconstruction of tracts in a 3D field has previously been used to examine the tongue [34-37]and white matter tracts in the brain [33, 38]at a high level of detail. In previous studies, histological and DTMRI (diffusion tensor MRI) have been used to study the tongue and infracted myocardium but lack the highly resolved tractographic capability of DSI. Used here, DSI is capable of extracting cardiac muscle fiber orientation based on diffusion strength and direction and then translating cellular alignment into tissue structure, thereby providing a basis for comparison of normal and abnormal myocardium.

1.6 Impaired myoarchitecture and associated mechanics

A digression from normal cardiac myoarchitecture is believed to be associated with impaired mechanics, and by extension, congestive heart failure. The two proposed cases discussed in this thesis, myocardial infarction with subsequent ventricular wall remodeling, and gene deletion of filament protein cMyBP-C, have been hypothetically linked with myoarchitectural disarray and pump failure. Whether the fiber abnormality takes place as a result of an injury to a fully developed heart or as a genetic mutation in an immature heart, the deviation from normal fiber alignment caused by molecular alterations provides a link to organ scale dysfunction.

It is generally accepted that alignment of cardiac myocytes during remodeling dictates its myoarchitecture and thus, is coupled with alterations of mechanical strain [21, 39]. In the first goal of this study, DSI with tractography is used to examine the myofiber architecture of normal and infarcted hearts to provide insights to the process of tissue remodeling and how the formation of fiber structures affects cardiac mechanics. The second goal of this study was to investigate the impact of cMyBP-C on macroscopic myocardial architecture and its role in cardiac mechanics. DSI reflects the principal directions of proton diffusion within myocytes whereas two-photon microscopy (TPM) depicts the morphology and mean alignment of a set of individual muscle fibers. Together, with streamline tractography, a multi-voxel and multi-scale representation of fiber architecture can be inferred. The use of DSI and TPM here serves as an intermediary measurement of local deformation and link to molecular and cellular changes such as shortened systolic ejection time and lengthened diastolic relaxation time.

Chapter 2

Methodology

2.1 Animal preparations

2.1.1 Normal and infarcted rat hearts

Hearts were excised from four normal and four infarcted age-matched rat hearts. DSI tractography and histology (H and E, and Mason's trichrome staining) were performed on the normal and infracted hearts. Normal hearts were fixed by canulating the inferior vena cava and infusing the myocardium with a 4% paraformaldehyde solution and then excised under deep anesthesia. Upon removal, all hearts were fixed in a 1% paraformaldehyde solution.

2.1.2 Induction of infarction in rat heart

Infarction was induced by permanent suture ligation of the left anterior descending coronary artery. After three weeks, the infracted hearts were perfused-fixed and excised following the same protocol as described for normal hearts. For histology, the hearts were cut longitudinally along the horizontal long axis in the 4-chamber view in 5 μm sections starting from the anterior free wall surface of the left ventricle.

2.1.3 Wild type and cMyBP-C$^{-/-}$ mouse hearts

Excised hearts from one wild type and three cMyBP-C$^{-/-}$ male mouse hearts were studied and imaged using DSI tractography. One wild type and knockout heart were then imaged using two-photon microscopy. Adult mice (8 to 36 weeks old) were injected with heparin for euthanasia and anesthetized with isoflurane for rapid extraction of the hearts. Upon extraction, hearts were fixed in buffered neutral 10% formalin.

2.1.4 Gene deletion preparations of the cMyBP-C$^{-/-}$ mouse hearts

The goal of this experiment was to characterize and quantify the myoarchitectural defect associated with the cMyBP-C gene deletion. The method to produce mice lacking the cMyBP-C gene was previously published [29]. In brief, homozygous cMyBP-C null mice by deleting exons 3-10 from the endogenous cMyBP-C gene and replacing those exons with a neomycin resistance gene. The resulting targeting vector was electroporated into two separate 129/Sv ES cell lines. Following characterization, the targeted clones were used to generate chimeric founder mice. It has been shown that cMyBP-C expression in heterozygous mice does not differ from wild type mice, and therefore one functional allele provides sufficient compensation. cMyBP-C$^{-/-}$ mice survived through senescence and were fertile. Reverse transcription PCR, performed to 3' regions of cMyBP-C cDNA, was implemented to identify the absence of cMyBP-C RNA expression in cMyBP-C$^{-/-}$ mice. As expected, results showed that the 345-bp product from exons 3 to 10 in wild type and heterozygous cDNA was not detected in homozygous cMyBP-C$^{-/-}$ cDNA [29]. Furthermore, Western blot analyses using a polyclonal antibody against rat cMyBP-C confirmed the absence of cMyBP-C in the cardiac myofibrils of homozygous mouse hearts. The full-length 150 kDa cMyBP-C band present in wild type and heterozygous hearts was not detected in

the cMyBP-C$^{-/-}$ hearts. Although cMyBP-C isn't required for cardiac development, mice 3 weeks old displayed significant cardiac hypertrophy. Furthermore, it was shown that there was no compensatory expression of skeletal MyBP-C isoforms in the heart.

2.2 Methods for imaging cardiac myoarchitecture

Cardiac preparations were imaged to delineate mesoscale myoarchitecture through the following methods: 1) Diffusion spectrum imaging (DSI), 2) High speed multi-slice, two photon microscopy (TPM), and 3) Generation of tractography from DSI and TPM datasets.

2.2.1 Diffusion Spectrum Imaging (DSI)

DSI tractography is an imaging technique capable of resolving multiple diffusion vectors per voxel [34, 40]. By measuring microscopically resolved 3D diffusion functions and macroscopically reconstructing myofibers using tractographic methods, DSI provides a structure template for local deformation and mechanical function. DSI tractography is based on the measurement of principal diffusion vectors from magnetic resonance imaging (MRI) as previous described in [36, 41]. MRI is a non-invasive imaging technique, which utilizes the nuclear magnetic resonance phenomenon to produce an image. By applying pulsed magnetic field gradients in the setting of a homogeneous magnetic field, nuclear spins acquire spatially dependent frequency and phase [42]. The resulting time domain signal has a Fourier transform relationship with spatial properties of biological tissues. One mechanism by which MR contrast is obtained is through diffusion weighting, in which the signal intensity is attenuated quantitatively by diffusion in a specific direction and then collected in an array of spatially aligned diffusion signals to create an image. The MR scanning pulse sequence is a time dependent series of magnetic field gradients applied in various spatial directions. This enables the

interrogation of internal variables of the system, such as diffusion. Diffusion defines the random motion of molecules and can be observed in all physical states of matter. In single-phase diffusion (as in employed during diffusion weighted MRI), molecules move about within the same phase, a condition termed homogeneous or self-diffusion. Although the diffusion of molecules is equally probable in all directions, the presence of barriers such as cell walls induces a principal direction of diffusion (Fig 2.2.1). Therefore, the elongated cylindrical geometry of cardiac muscle cells directs diffusion along the myofiber axis rather than perpendicular to it [43, 44].

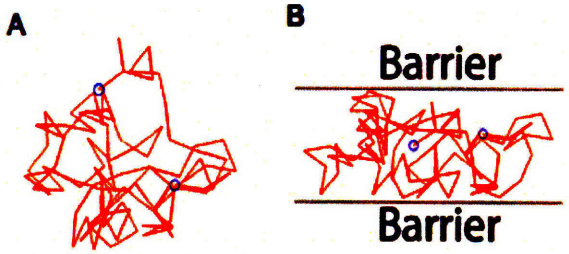

Figure 2.2.1. Principles of diffusion. (A) Direction of random diffusion is equally probably in all directions. (B) The cell walls of myocytes direct diffusion preferentially in the direction of the fiber axis (left of right).

Diffusion weighted MRI specifically images water molecules whose displacement is constrained by one or several biological boundary conditions, such as membranes [45-47].

In Figure 2.2.2A, a set of two fiber populations are illustrated with crossing fibers within a voxel. Physical fibers imaged with DSI are translated into a q-space [34, 36, 37](Fig. 2.2.2B), a per voxel map of MR signal intensities representing the total diffusivity based on the magnitude and direction of an applied magnetic field. In q-space, the signal is weakest in the direction of the myofiber and strongest when orthogonal to the fiber direction. In other words, highly anisotropic diffusion of water molecules in myofibers equates to weaker MR signal intensities. An inverse Fourier transform of q-space (q-value) produces a complete

probability density function (PDF) (Fig. 2.2.2C) for diffusing protons in a tissue per voxel as shown by,

$$\bar{P}_S(\vec{R},\Delta) = F^{-1}[M(\vec{q},\Delta)] \tag{2.2.1}$$

where $\bar{P}_S(\vec{R}|\Delta)$ represents the three dimensional PDF, summed over each proton spin position and weighted by the proton density distribution over diffusion time Δ, diffusion distance $\vec{R}$, and q-value $\vec{q}$. Known Bloch Torrey equations [48,49] were further modified by Stejskal to account for the general anisotropic diffusion and velocity due to the diffusion equation [50, 51], relating $\bar{P}_S(\vec{R}|\Delta)$ to signal attenuation $M(\vec{q},\Delta)$ over the applied diffusion weighting gradient $\vec{g}$ and time as,

$$M(\vec{q},\Delta) = M(\vec{0},\Delta)\int \vec{P}_S(\vec{R}\,|\,\Delta)e^{(i\vec{q}\cdot\vec{R})}d\vec{R} \tag{2.2.2}$$

$$\vec{q} = \gamma\vec{g}\delta \tag{2.2.3}$$

where γ is the proton gyrometric ratio. The PDF thereby reflects the fiber orientation within a voxel and the likelihood of diffusion in a particular direction and distance. This is then translated into an orientation distribution function (ODF) by radial integration (Fig. 2.2.2D),

$$ODF(\hat{u},\Delta) = \int \bar{P}_S(\rho\hat{u},\Delta)\,\rho\hat{u}\,d\rho \tag{2.2.4}$$

to depict the fiber architecture as a function of only fiber angle. The ODF is weighted by the magnitude ρ and unit vector $\hat{u}$ of $\vec{R}$.

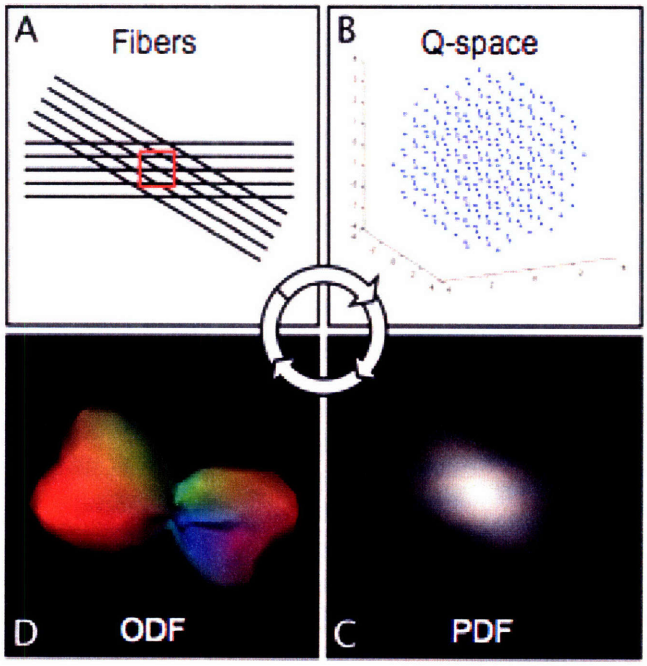

Figure 2.2.2. Derivation of fiber orientation from DSI [41] (A) Illustration of a set of two crossing fiber populations within a voxel (red box). (B) Fibers are translated into a q-space representing MR signal intensities. (C) Through an inverse Fourier transform, a PDF is calculated. (D) Representing actual fiber alignment seen in (A), the ODF is derived by radially integrating the PDF.

Magnetic resonance imaging protocols:

The imaging protocol employed a diffusion gradient sampling scheme, which consisted of a key-hole Cartesian acquisition to include q-space values lying on a Cartesian grid within a sphere for a total of 515 diffusion weighted gradient vectors.

Protocol for imaging rat hearts:

A 4.7T horizontal bore magnet (Bruker Biospec) with a 120 mm internal diameter and 10-turn solenoid radiofrequency coil was used to image the normal and infarcted rat hearts. The hearts were immersed in Fomblin oil and imaged with a maximum b-value of 10^4. A voxel size of 0.4mm was achieved with an approximate imaging time of 10-12 hours per sample.

Protocol for imaging mouse hearts:

Imaging experiments of the mouse hearts (wild type and knockout cMyBP-C$^{-/-}$) were performed using DSI tractography at 9.4T with a horizontal bore magnet (Magnex Scientific) equipped with a Magnex gradient coil set with capabilities up to 20 G/cm. All the hearts were immersed in Fomblin oil and imaged with a maximum b-value of 4000. To achieve a voxel size of approximately 0.16 mm for the wild type and knockout mouse hearts, the approximate imaging acquisition time took 10-12 hrs per sample.

2.2.2 Two-photon Microscopy (TPM)

The use of 2-photon microscopy was employed to confirm the myoarchitecture obtained with DSI of wild type and knockout mouse hearts. Following DSI, the hearts were sectioned for two-photon microscopy. TPM was employed to visualize microstructure of the ventricular wall of cardiac tissue. Compared with confocal microscopy, TPM typically has larger imaging depth up to 1 mm.

Protocol of imaging wild type and cMyBP-C$^{-/-}$ mouse hearts:

To reconstruct a 3D model representing fiber orientation based on an autocorrelation program from TPM images [36], the tissue was sectioned and imaged in slices with a thickness 30 μm. The excised hearts were prepared by fixing the samples in buffered neutral 10% formalin post imaging and then embedding them in paraffin. The embedded samples were cut longitudinally from base to apex along the septal wall, thereby isolating the left ventricle, and fixed on the sample stage. A total sample size of approximately 1mm x 1mm x 1mm was imaged at 10 frames per second for 300 x 400 pixels using a one color channel. TPM was

performed with 14 fields of view (steps) in the x-direction, 18 in the y-direction, and 30 in the z-direction.

TPM to determine 3D myoarchitecture:

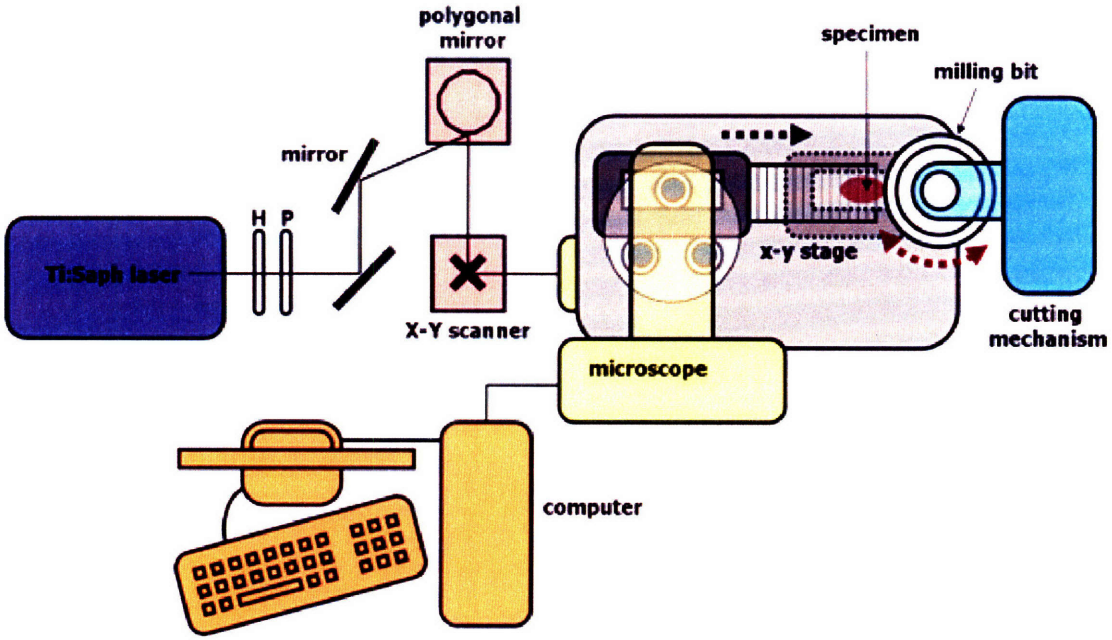

Figure 2.3.1 Experimental setup of 3D TPM. This system consists of a high speed TPM scanning apparatus based on a spinning polygonal mirror, automated x-y specimen stage control, and a precision specimen mechanical cutting mechanism. H denotes half-wave plate and P denotes polarizer. Custom software was used for automated control of stage position, cutting, and data acquisition.

Left ventricular wall specimens of both wild type and knockout mice were imaged using a customized multi-photon high speed imaging system set up around a Zeiss microscope (Axioscope, Zeiss Thornwood, NY) with an automated x-y specimen stage, an automated tissue cutting mechanism, and a high speed polygonal scanning mirror (Fig 2.3.1) [52, 53].

The main concepts underlying the two-photon microscopy technique have been previously discussed in detail [36, 41, 54]. Because the tissue area of interest was larger than the field of view

of the microscope objective, a robotic stage (H101, Prior Scientific, Rockland MA) was used to position the sample for each image. Furthermore, the objective was mounted on a computer-controlled piezoelectric objective translator (P-722.00, Physik Instrumente, Waldbronn, Germany) and axially translated to acquire a z-stack of image planes, here used to image a depth of 60 μm. To image the full 3D section of the ventricular wall, parallel 30 μm layers of tissue were removed continuously after each individual layered was imaged from the epicardial to endocardial surface.

A femtosecond Ti: Sapphire laser, powered by a continuous wave Nd:YLF diode pump laser, (Mira 900, Coherent, Palo Alto, CA) was used to induce two-photon fluorescence, providing high power mode-locked pulses for non-linear two photon excitation. The microscope system was optimized for excitation in the range of 700 - 900 nm. A half wave plate (CVI Laser Inc., Putnam, Connecticut) and a Glan-Thomson polarizer controlled both the polarization and the excitation power. Using two different scanners — a slower galvanometer-driven scanner with 500 Hz bandwidth (Cambridge Technology, Cambridge, MA) and a fast rotating polygonal mirror (Lincoln Laser, Phoenix, AZ) — the laser beam is rapidly raster scanned across a sample plane. The galvanometer-driven scanner performs line-scanning along the y-axis. The polygonal mirror, composed of 50 aluminum-coated facets arranged side by side around the perimeter of the disc, performs high speed line-scanning along the x-axis. The position of the mirror was encoded by an independent laser diode (1mW at 632 nm, Thorlabs, Newton, NJ) along with a photodiode detector (Thorlabs). An imaging rate of 10 frames per second, 0.7 μs pixel residence time, and a 3750 rpm rotation speed, resulted in a line-scanning speed of 320 μs/line.

The microscope (Axioscope, Zeiss, Thornwood, NY) was coupled with a laser beam through a modified epiluminescence light path, which directed a beam reflected by the dichroic mirror towards the objective (Zeiss 40× Fluar 1.3 numerical aperture (NA)) and focuses it on the specimen. Non-spatially resolved detectors (R3896, Hamamatsu, Bridgewater, NJ) were used to collect the emitted photons. The induced fluorescence signal passed through the same dichroic mirror and was collected by the same objective. An additional barrier filter (SP700, Chroma Technology, Brattleboro, VT) is used to remove scattered light.

The signals resulting from the PMT were converted into a voltage signal using a trans-impedance circuitry and a 16-bit A/D converter (NI 6251, National Instruments Corp., Austin, TX) and transferred to the computer memory using a PCI bus. Integrating the signals synchronized with the x-y scanning patterns generates microscopy images. The x-y scanners, microscope objective translator, and PMT detection system were synchronized using a high-speed data acquisition circuit and reference signal produced by the independent laser diode used to position the polygonal mirror.

Post acquisition handling of TPM image datasets:

Following the acquisition of the 3D dataset via TPM, a 3D autocorrelation algorithm was performed to extract the main fiber directions per voxel in microscopic fields of view (FOV) [36, 41], resulting in a track file also processed in Diffusion Toolkit and TrackVis. Each FOV was divided into four individual image volumes with voxel size 60 μm x 60 μm x 60 μm. The image volumes were initially linearly interpolated in the z-direction to achieve isotropic voxel resolution. Each image volume file was translated into a set of 181 equally spaced

vectors on the surface of a half sphere, where a single value was extracted and recorded from the bidirectional radial integration. To reduce edge effects of restacking the TPM images, a Kaiser window was applied to the image volumes. Through a 3D Fourier transform, the data is then displayed in a frequency space, and a frequency filter was then used to remove features/signals with wavelengths greater than or equal to 120 μm. The Fourier transform of the image volume was calculated through a component by component multiplication of its conjugate to obtain the autocorrelation [41], and then followed by an inverse transform back into real space as shown below:

$$Acorr = F^{-1}(G \cdot \bar{G}) \tag{2.2.5}$$

where G is the 3D Fourier transform of the image volume, and $\bar{G}$ is the complex conjugate of G. By radially integrating from the center of the autocorrelation data, an ODF like that resulting from DSI tractography is created, depicting the mesoscale muscle fiber orientations (Fig. 2.3.2). The principal fiber directions calculated from autocorrelation analysis were then compared to the diffusion vectors associated with DSI.

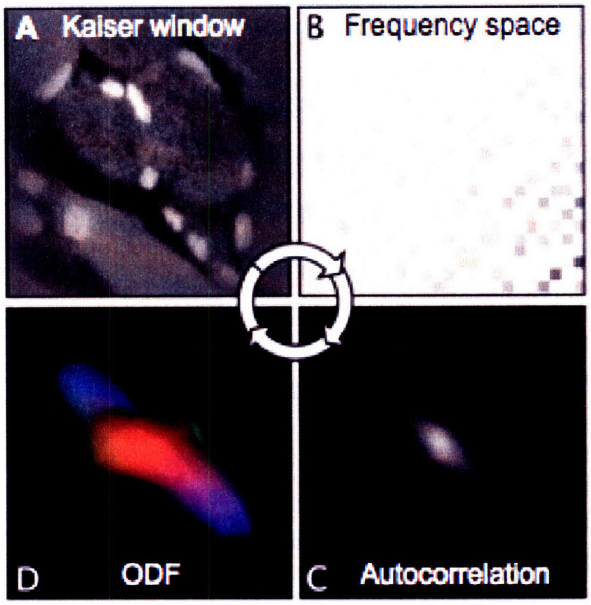

Figure 2.3.2 Derivation of fiber orientation from TPM [41]. (A) A Kaiser window is applied to reduce the edge effects of z-stacking the microscopy images. (B) A 3D Fourier transform depicts the data in a frequency space. (C) The autocorrelation is calculated by multiplying the 3D transform by its own complex conjugate. (D) A radial integration of (C) results in an ODF.

2.2.3 Generation of tractography from DSI and TPM

DSI and TPM datasets were processed using custom software, Diffusion Toolkit and Trackvis (trackvis.org), to reconstruct and visualize the 3D myocardial architecture. Fiber tracts were constructed based on the vector directions in the ODF. Streamline construction, $\vec{S}$, generates continuous multi-voxel tracts that follow the direction of the maximal diffusion vectors [41]:

$$\frac{d\vec{S}(s)}{ds} = \vec{v}(\vec{S}(s)) \qquad (2.2.6)$$

where s is a path coordinate along $\vec{S}$ and $\vec{v}$ is the vector field. The streamline vector field was calculated from the set of largest eigenvectors from the diffusion tensors of each voxel. Intervoxel connectivity was formed when vectors lie within an angular threshold of +/- 17.5°, taking the path of minimal angular difference. When the streamline vectors exceeded

this range, the tracts were discontinued. Streamline tracts are generated from the center of each voxel and connected in any direction within the threshold.

For all hearts, the visualization of myofibers in TrackVis is depicted using a helix color-coding scheme, where yellow/green indicates a negative left-handed helix angle and dark blue/pink indicates a positive right-handed helix angle. The reference axis lies longitudinally from base to apex of the heart. For the following analyses, a region of interest (ROI) sphere of a specified radius was used to isolate and visualize fibers in the myocardium.

Chapter 3

Myoarchitecture of normal and infracted myocardium

In this chapter, DSI tractography is applied to four normal and four infarcted rat hearts. The results reveal unique aspects regarding normal cardiac myoarchitecture and remodeling. The myocyte fiber patterns are related to the mechanism of contraction and relaxation.

3.1 DSI tractography of the normal rat heart

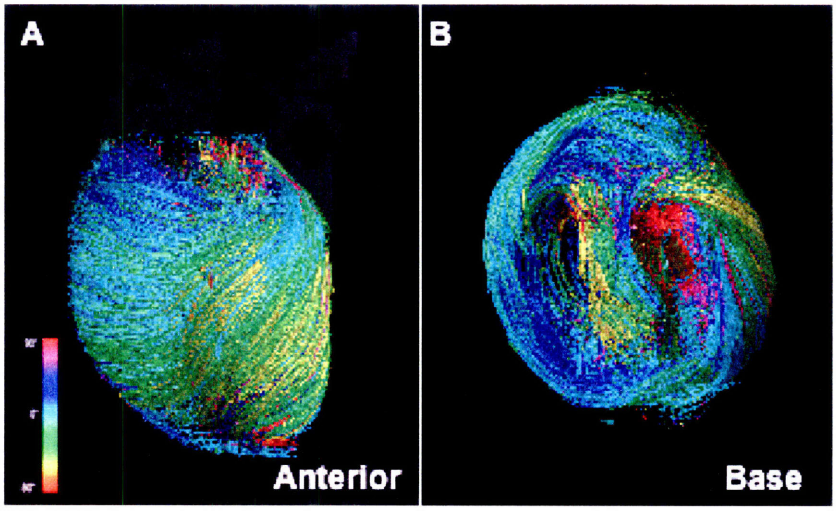

Figure 3.1.1. DSI tractography of normal rat heart shown from the (A) anterior and (B) base. The myoarchitecture of the right and left ventricle separated by the septal wall is shown. The fibers are colored by helix angle and vary mostly as a function of ventricular wall depth.

Through DSI tractography, tracts reconstructing the alignment of cardiac muscle fibers result in a mesoscale depiction of the normal heart (Fig. 3.1.1). From both the anterior and basal view, the right ventricle is located on the left hand side, while the left ventricle is on the right hand side. In Figure 3.1.1A, the base of the heart is located at the top of the diagram, and the apex at the bottom. The depiction of the cardiac myoarchitecture from the base illustrates and confirms that the left ventricular wall is much thicker than that of the right. In addition, the left and right ventricles share the tracts that form the septal wall. The fiber helix angles along the left ventricular wall vary mostly as a function of depth from subepicardium to subendocardium from negative to positive angles, respectively. From the basal view of this particular heart, circumferential (light blue) fibers encircling the entire heart seem to dominate the myocardium.

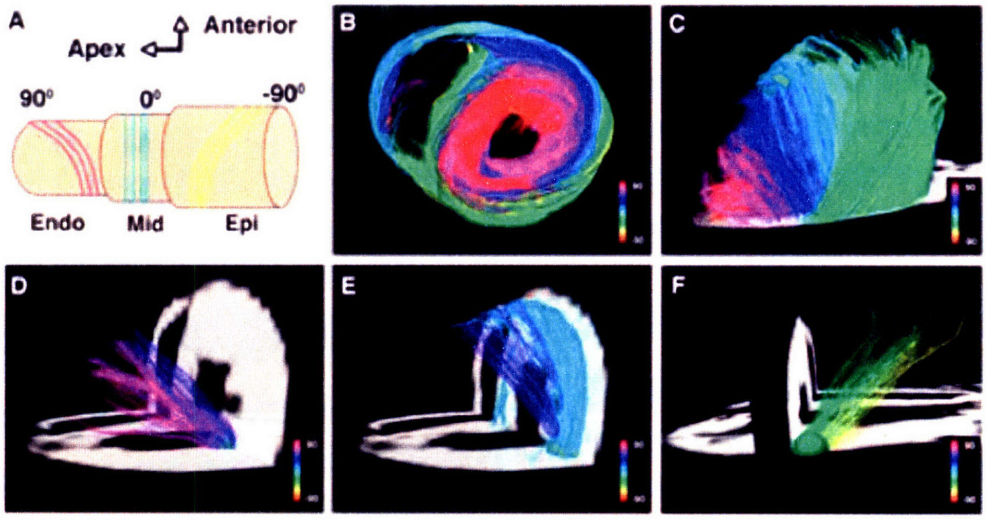

Figure 3.1.2. Fiber helix angle of normal myocardium. (A) Helix color scheme as seen from the lateral wall of the left ventricle. Myocardium viewed from the (B) short axis/base and (C) lateral wall display a smooth gradient of helix angles from subepicardium to subendocardium. (D) Positively angled subendocardial (pink) fibers point towards the apex. (E) The midmyocardium consists of circumferential (light blue) fibers. (F) Negatively angled subepicardial (green, yellow) fibers point towards the base.

DSI tractography of normal myocardial architecture confirms previous studies illustrating the continuous gradient in fiber helix angle as a function of ventricular wall depth. Using helix angle color encoding, the fiber tracts along the left ventricular wall gradually transition from helices with negative angles in the subepicardium to zero degrees (circumferential) in the midmyocardium to positive angles in the subepicardium (Fig. 3.1.2). The left-handed helices in the subepicardium point towards the base, while the right-handed helices in the subendocardium point towards the apex.

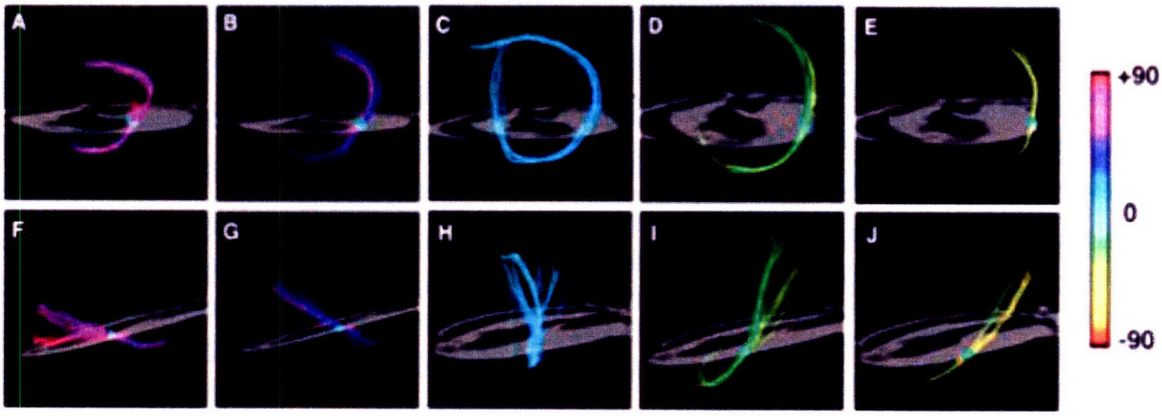

Figure 3.1.3.Gradient of helix angles in the left ventricular wall. Panels (A) to (E) viewed from the apex and panels (F) to (J) viewed from the lateral wall display isolated fibers intersecting with a ROI sphere from the subendocardium to the subepicardium, respectively.

By using a ROI sphere to isolate fibers along the left ventricular wall, Figure 3.1.3 shows that the change in helix angles from negative to positive occurs continuously and gradually. The pink subendocardial fibers in Figure 3.1.3A display an angle of about -66°, the light blue midmyocardial fibers in Figure 3.1.3C are 0°, and the yellow subepicardial fibers in Fig 3.1.3 E are about 57°.

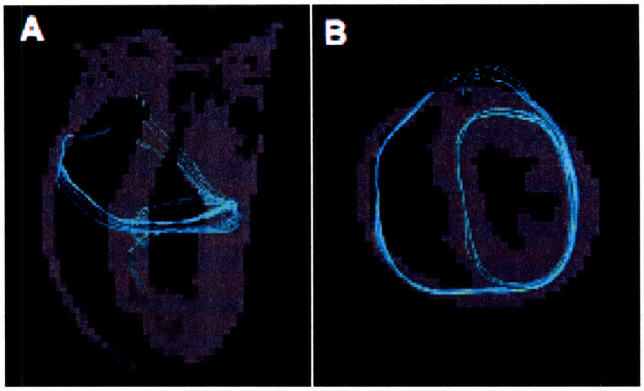

Figure 3.1.4. Orientation of isolated midmyocardial fibers. A population of midmyocardial and subepicardial fibers encircle both the left and right ventricle, forming a torus knot-like shape.

In addition, midmyocardial and subepicardial fibers spiral around the left ventricle, cross at the septum, and make up a portion of the right ventricular wall (Fig. 3.1.4). This fiber pattern can be compared to a torus knot. A projection of the myocardium from the anterior and lateral walls of the left ventricle shows subepicardial (green-yellow) and midmyocardium (light blue) fibers arranged in a dense, organized sheet-like manner (Fig. 3.1.5). A histological section performed on the corresponding location shows a high degree of correlation with similar fiber orientation in the left ventricular myocardium.

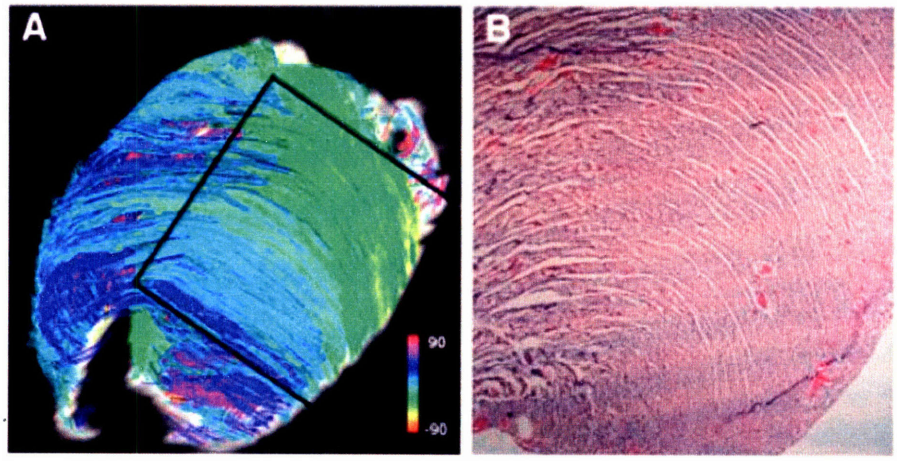

Figure 3.1.5.Myofiber architecture in a normal rat heart. (A) Projection of left ventricle from anterior and anterolateral walls. The subepicardial and midmyocardial fibers viewed in the black box are consistent with the fibers seen in the histological section (B).

3.2 DSI tractography of an infarcted heart

Post infarction, the hearts are characterized by ventricular wall thinning and rounding of the heart as well as disrupted irregular myofiber architecture around the infarct zone. More specifically, the infarct zone is replaced by a fiber void in the anterolateral apex (Fig. 3.1.6).

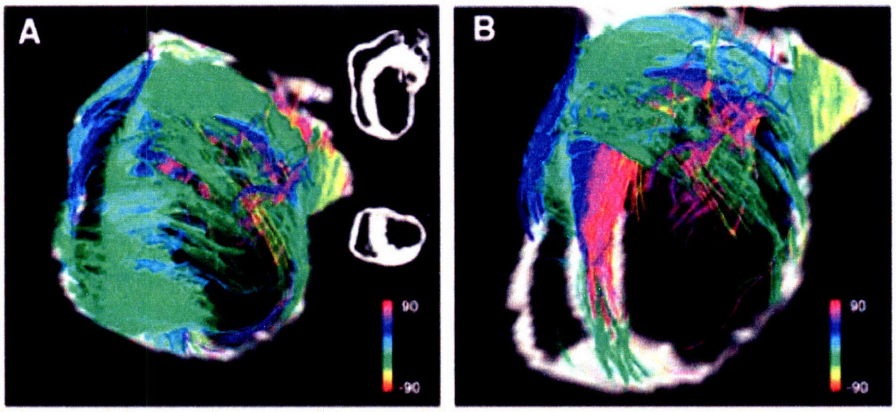

Figure 3.1.6. DSI depiction of myofiber architecture post infarction. (A) Viewed from the anterior wall of the left ventricle, a fiber void is apparent in the infarct zone, particularly in the anterolateral apex. (B) A DSI reconstruction through the infarct shows irregular fibers penetrating past the basal and septal border.

On the other hand, myofiber strands frequently penetrate the border zone (infarct boundary) from the base and septal wall, forming an irregular mesh-like structure in the upper half of the infarct area. This mesh structure is composed of subepicardial (green) and midmyocardial (light blue) fibers oriented transversely from the septal wall and subendocardial (pink) fibers running longitudinally from the basal border. The Mason's trichrome showed similar signs of the growth of transverse myofibers past the border zone, where the myofibers were stained brown and collagen blue (Fig. 3.1.7). The subendocardial longitudinal fibers are confirmed in a corresponding H and E histological section, showing the growth of myofibers from the basal perimeter of the infarct.

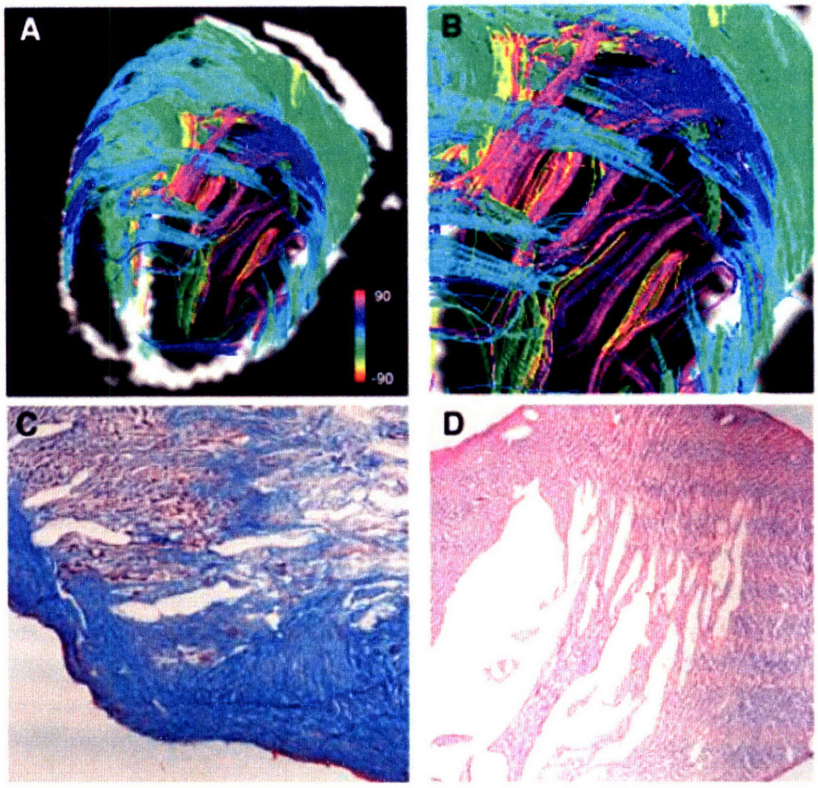

Figure 3.1.7. DSI tractography and corresponding histological sections of the infarct. (A) The infarct zone from a different heart is characterized by penetrating fibers. (B) A magnified view of (A) shows that these fibers consist of longitudinal pink subendocardial fibers extending from the basal border as well as transverse midmyocardial light blue and subepicardial green fibers extending from the septal border. (C) The presence of transverse fibers is confirmed in the Mason's trichrome, where the myofibers are stained brown and collagen blue. (D) The longitudinal fibers are confirmed in the H and E sections.

As with the normal myocardium, 2D histology images correlated with DSI images, showing the presence of penetrating myofibers in the infarct zone.

3.3 Impact of myocardial infarction on remodeling and mechanics

The depiction of gradually changing helix angles from subepicardium to subendocardium suggests that the normal myocardial architecture is organized in the form of laminar sheets

consisting of helical fiber tracts. Because fiber tracts are shared between the left and right ventricle in addition to the septal wall, cardiac function of the ventricles are functionally connected, thus allowing shared fibers to be involved in the transfer of force from one ventricle to the other. Accordingly, a change in left ventricular fiber orientation such as that associated with infarction impacts the contractile function of both ventricles. DSI represents the myocardium as a collection of the spiraling myofibers around the heart, which plays an important role in normal mechanics of ventricular contraction and relaxation [9,20].

The ischemic zone of the infarcted myocardium is characterized by a lack of diffusion or reduced diffusional anisotropy, as illustrated by the fiber void. Particularly near the anterolateral apex, the fiber void indicates the replacement of normal tissue with collagneous scar tissue, which lacks diffusion and helical orientation. The use of DSI on infarcted hearts illustrates the formation of an intersecting mesh made up of longitudinal and transverse fibers penetrating the border zone. The growth of both subepicardial and subendocardial fibers in seemingly equal proportions confirmed by histology reflects similar susceptibility to infarction injury as well as the importance of both to cardiac function. Because the subendocardial surface sustains greater wall stress than the subepicardial surface [55], it's hypothesized that the growth of longitudinal fibers is strongly induced and necessary to balance the stress placed on the surrounding tissue. On the other hand, normal contractile twisting follows the left-handed helical direction of subepicardial fibers [3], and therefore, the growth of subepicardial transverse fibers is promoted to regain a degree of normal contractile motion.

It is possible that the mesh-like structure provides tensile strength to the myocardium and prevents infarct expansion [56]. Furthermore, the penetrating myofibers help prevent the thinned injured ventricular wall from erupting due to pressure from the rhythmic contraction and relaxation of the heart. It may act as a remodeling step, in addition to the hypertrophy of the surrounding ventricular walls, to help compensate for the decrease in wall strength and force. However, while the presence of these intersecting myofibers may serve as a mechanical advantage, it may also be highly susceptive to electrical re-entry and vascular tachycardia [57].

Chapter 4

Relationship between cMyBP-C expression and cardiac myoarchitecture

In this chapter, the myoarchitecture of wild type and cMyBP-C knockout mouse hearts are illustrated and related to mechanics. The application of DSI and TPM is novel to cMyBP-C$^{-/-}$ hearts and reveals trends in fiber alignment that arise from molecular changes, leading to hypertrophic cardiomyopathy.

4.1 DSI and TPM tractography of wild type myocardium

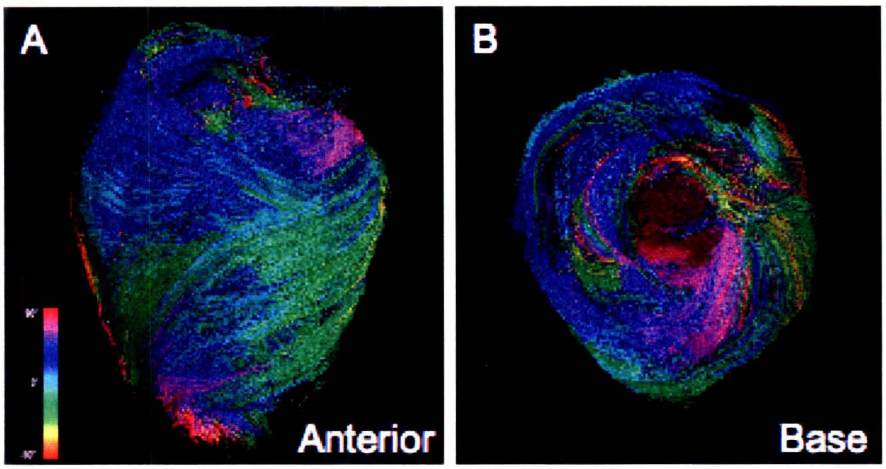

Figure 4.1.1. DSI tractography of a wild type mouse heart from the (A) anterior and (B) base. The fibers are color encoded by helix angle, displaying varying angles throughout the ventricular walls.

The wild type myocardium shows similar patterns as previously described for the normal rat hearts [4, 5]. In Figure 4.1.1, the wild type myocardium is shown from the anterior and basal view. The various helix angles can be seen by the variance in fiber tract color along the ventricular wall and as a function of wall depth from subepicardium to subendocardium. As a whole, the helix angles are generally consistent around the circumference of the ventricular walls and increase gradually while moving deeper into the wall. Although the left ventricular wall is much thicker, helix angles in the right ventricular wall vary similarly, but on a smaller scale. Reconstruction of TPM images from one wild type heart displays comparable changes in helix angle (Fig. 4.1.2).

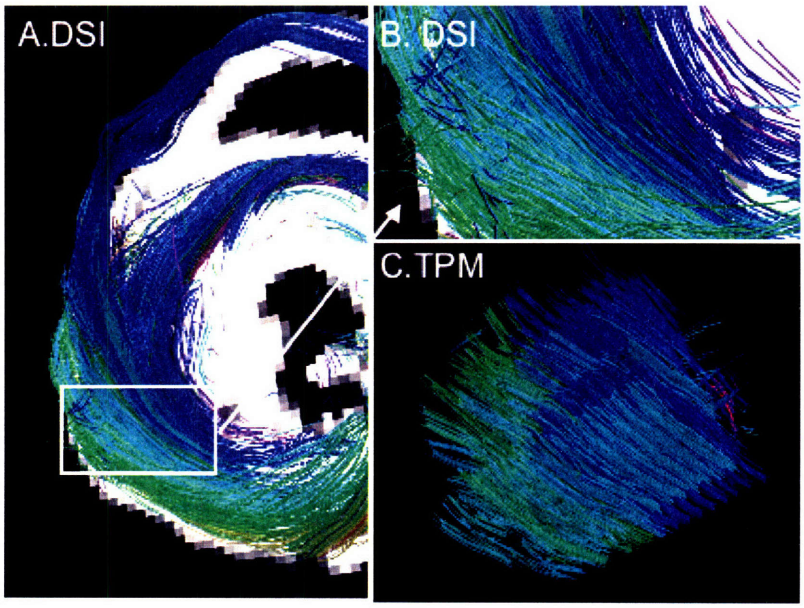

Figure 4.1.2. Comparison of DSI and TPM tractography of a wild type myocardium. (A) DSI projection of isolated fibers along the left and right ventricle as viewed from the base. (B) The corresponding imaged TPM location in DSI is magnified from (A) (white box). (C) Oriented similarly, TPM reconstruction of fibers shows similar helix angle variations as DSI (B) from the subepicardium to subendocardium.

Fig 4.1.2 isolates the TPM imaged area of left ventricular wall from the basal view of the DSI tract and shows that the TPM tract is similar to the DSI tract. DSI and TPM tracts here show similar patterns in tract color and orientation. Helix angles transition from negative

helices in the subepicardium (green) to circumferential helices in the midmyocardium (light blue) to positive helices in the subendocardium (dark blue). Because the parallel TPM slices were taken perpendicular to the long axis of the myocardium and not tangent to the fiber "shells", each slice contains portions of the subepicardium, midwall, and subendocardium. Specifically, the top slice displays midwall fibers (because the subepicardial surface was cut off during alignment of microscope), the middle slices display both subepicardial and midwall fibers, and the bottom slices contain both midwall and subendocardial fibers. Corresponding TPM sections on the DSI tract using ROI spheres were isolated, depicting four slices from the subepicardium to subendocardium with similar variations in helix angle and tract patterns (Fig. 4.1.3).

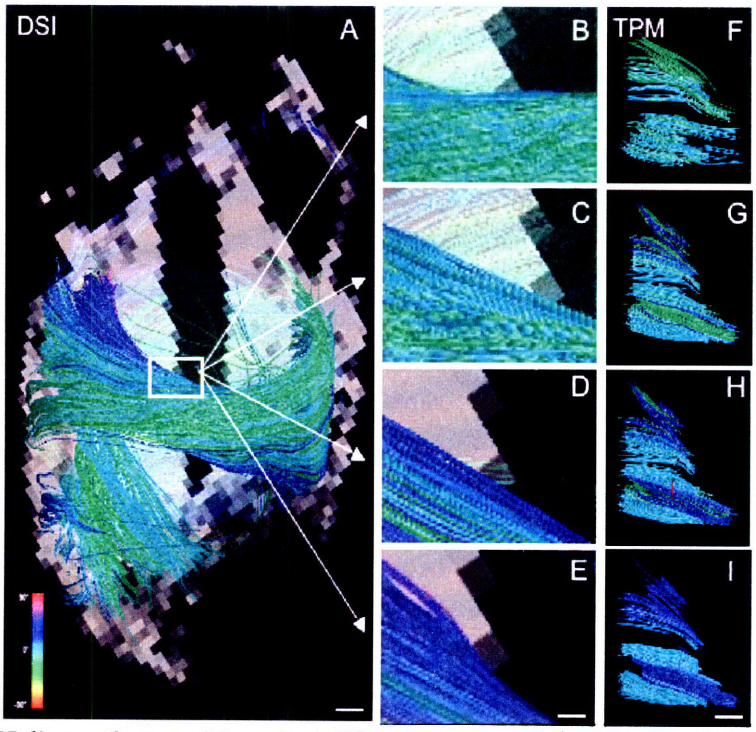

Figure 4.1.3. Helix angle transitions in wild type myocardium displayed by DSI and TPM tractography. (A) DSI visualization of full 2-chamber view from left ventricle of isolated myofibers imaged with TPM. White scale bar indicates 1 mm. (B-E) Enlarged DSI projections (white box (A)) illustrate the same gradient of fibers from positive to circumferential to negative helix angles as the (F-I) TPM images. For both (B-E) and (F-I), a ROI sphere was shifted parallel to the short axis from the subepicardium to subendocardium in each frame. White scale bar refers to 0.28 mm in (B-E), and 0.2 mm in (F-I).

The first slice in the subepicardium (Fig. 4.1.3B, F) consists of left-handed helices (green) and circumferential tracts (light blue). Right-handed helices (dark blue, purple) begin to dominate as the ROI sphere is shifted towards the subendocardium (Fig. 4.1.3E, I). The tracts shown by TPM change gradually from left- to right-handed tracts and follow the same pattern extracted from DSI tractography. Helix angles along the left ventricular wall were measured using an identical ROI sphere, showing similar gradients in helix angle from both TPM and DSI constructed tracts in Figure 4.1.4. The helical fibers change from -16° in the subepicardium to 0° along the midwall to 37° in the subendocardium. The myofiber patterns depicted by DSI are highly correlated to those found using TPM.

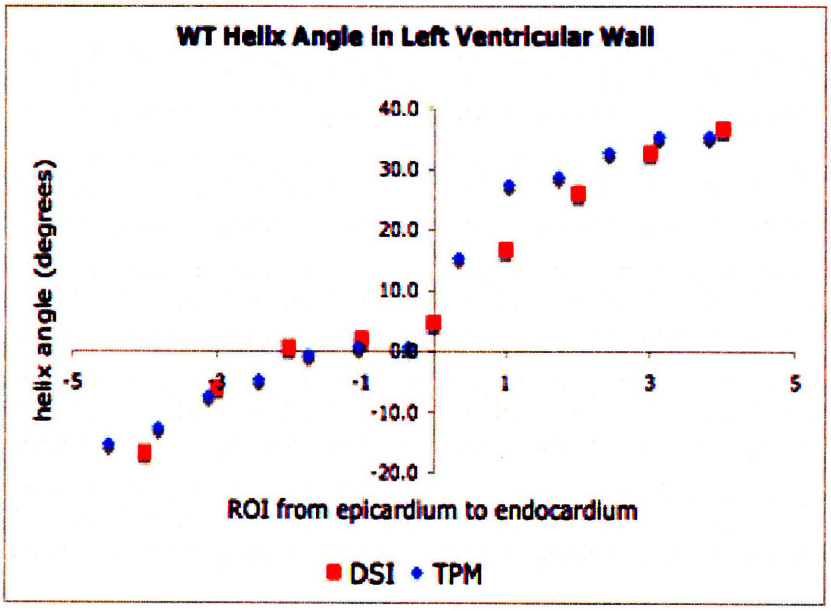

Figure 4.1.4. Plot of DSI and TPM fiber helix angle in the left ventricular wall from subepicardium to subendocardium of a wild type (WT) heart. Measured helix angles from DSI and TPM show a high degree of correlation and follow the same trend.

4.2 DSI and TPM tractography of cMyBP-C$^{-/-}$ myocardium

In the cMyBP-C$^{-/-}$ myocardium, the anterior and basal view (Fig. 4.1.5) shows varying colors signifying different fiber helix angles and appears similar in shape to the wild type myocardium. This particular knockout heart contains more circumferential fiber tracts and

less positive helix tracts (purple fibers). In addition, the overall myocardium appears slightly rounder, and the distinction between the ventricular and septal walls is less clear. The change in helix angle remains a function of wall depth as with the wild type.

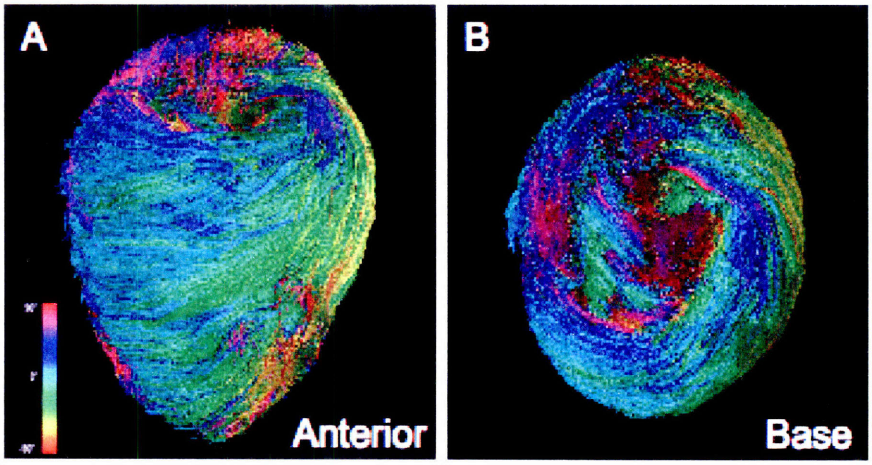

Figure 4.1.5. DSI tractography of a homozygous knockout cMyBP-C mouse heart from the (A) anterior and (B) base. The fibers are colored by helix angle and appear similar in shape to the wild type myocardium. Three knockout hearts were imaged with DSI.

Comparing the TPM and DSI tracts of the knockout myocardium (Fig. 4.1.6), the pattern of helix angles of the fibers is different from that in the wild type (Fig. 4.1.2). The corresponding tracts of the left ventricular wall are displayed for both DSI and TPM in Figure 4.1.6. The gradient in fiber colors is comparable between the two imaging methods. Rather than changing from green negative helix angles to light blue circumferential to dark blue positive helix angles (Fig. 4.1.2), the knockout fibers lack the gradual transition in angles. The subepicardial surface appears green and light blue, but the midwall fibers are dark blue, followed by positive purple, negative yellow and red helix fibers in the subendocardium.

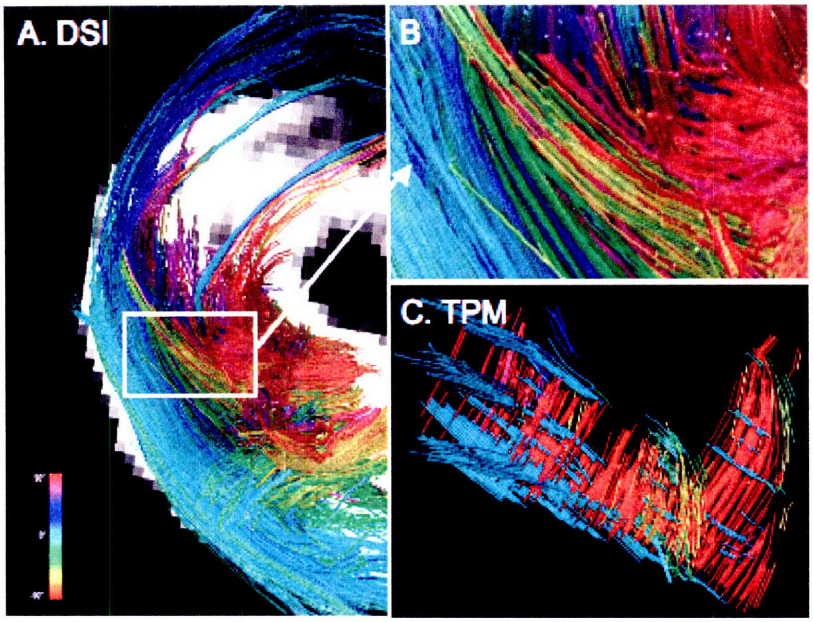

Figure 4.1.6. Comparison of DSI and TPM tractography of a cMyBP-C$^{-/-}$ heart. (A) DSI projection of left and right ventricle from a basal view. (B) Enlarged DSI image of tracts (white box (A)) corresponding to the imaged TPM location. (C) TPM reconstruction of fibers showing similar helix angle variations as DSI (B). The knockout tracts in both DSI and TPM show much more fiber disorder and different helix angle transitions than the wild type myocardium.

Compared to the wild type, the knockout myocardium appears less cohesive with much greater variances in tract orientation. The fibers lose the strongly negative helix angles on the subepicardial surface, but gain them on the subendocardial wall. As with DSI of the knockout heart, TPM generally displays inner wall tracts with helix angles at both extremely positive and negative ends of the color scale. The presence of circumferential fibers on the inner wall and perpendicular to the TPM slices further indicates fiber disorder in the knockout myocardium.

Upon closer inspection, measurements of fiber helix angle and average fiber tract length reveal fiber abnormalities in the knockout myocardium. The fiber tracts or intervoxel

diffusion coherence were extracted, comparing wild type and knockout mice (Fig. 4.1.7). A longer the fiber tract indicates a stronger diffusion signal and direction.

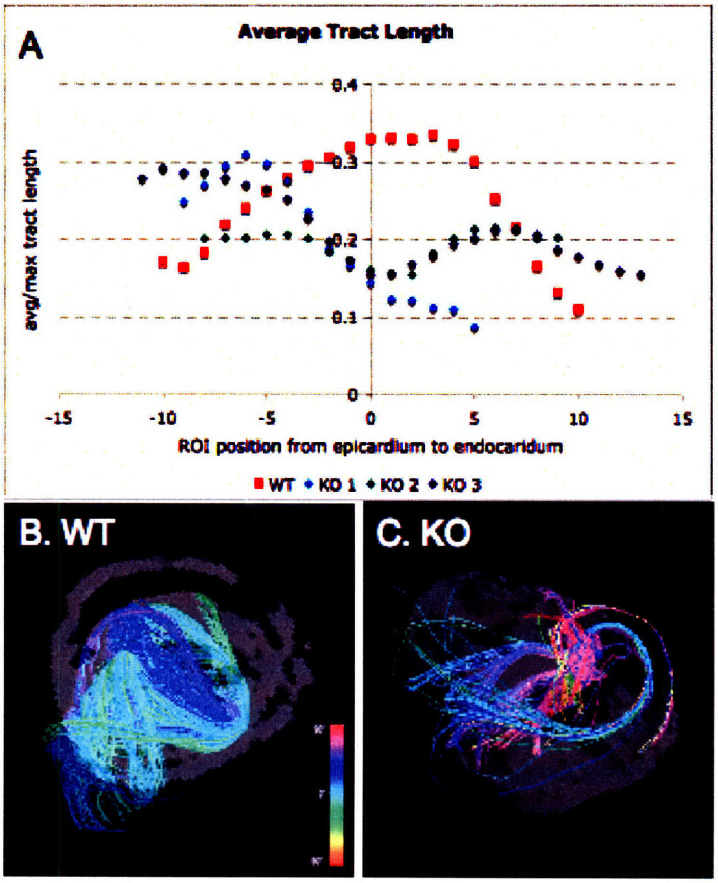

Figure 4.1.7. Average tract length and corresponding DSI projections. (A) Plot of average fiber tract lengths along the left ventricular wall for three knockout and one wild type mouse hearts. For normalization, the average fiber lengths are divided by the maximum fiber length measured for each specimen. At the midmyocardium, the wild type (WT) fiber length peaks, while the knockout (KO) fiber lengths reach a minimum. Using a ROI sphere, DSI images of the (B) WT and (C) KO are displayed at the midwall (position 0). The WT myocardium fibers appear dense, coherent and strongly aligned in the same helical pattern. The KO myocardium fibers, on the other hand, appear sparse, short and disorganized dissimilar helix angles.

The peak average tract length for the knockouts occurs earlier in the subepicardium around ROI position -6 to -4, where the corresponding tract length in the wild type myocardium is approximately equal. Moving towards the midwall, the average tract length for the wild type heart peaks while those for knockout hearts reaches a minimum. In the respective location in

the knockout hearts (ROI position 0), fibers tracts have decreased in length and have become disorganized. DSI projection of the wild type displays tightly packed tracts mostly with a circumferential orientation (Fig. 4.1.7B). The cMyBP-C$^{-/-}$ tract is characterized by a range of fiber colors at opposite ends of the helix color spectrum and inconsistent orientations, thereby resulting in disorder (Fig. 4.1.7C). Even though the knockout hearts have a thicker ventricular wall, the tract lengths become short in the midwall to subendocardium, or in other words, the tracts lose voxel to voxel coherence.

Promoted by the difference in average tract length of the knockout hearts, measurements of fiber helix angles were taken in an identical manner for both types of hearts. More specifically, at the intersection of the y- and z-midplanes, helix angle was measured and plotted as a function of wall depth, displaying the transition of fiber orientation (Fig.4.1.8).

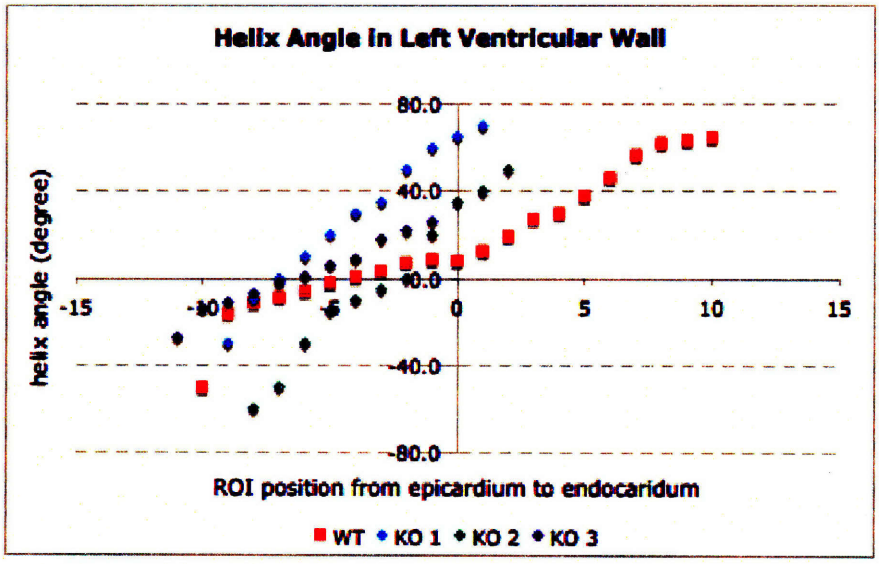

Figure 4.1.8. Helix angles in left ventricle of wild type and knockout hearts from DSI. Measurements were taken from three knockout and one wild type hearts from subepicardium to subendocardium. The fibers in the wild type myocardium follow a similar pattern as previously reported [4]. Overall, in the cMyBP-C-/- myocardium, the transition from negative to positive helix angles occurs faster and more linearly than the wild type and is restricted to the subepicardium. From the midmyocardium to the subendocardium, the helix angles were inconsistent and could not be measured.

Along the left ventricular wall, the helix angle changed symmetrically from left-handed helices to right-handed helices. In the wild type myocardium, the helix angle at the subepicardium of the left ventricular wall is measured as -55°, which gradually approaches 0° around the midwall to 70° in the subendocardium as shown in Figure 4.1.8. The fiber orientation changes rapidly in the subepicardium and subendocardium, and more gradually around the midmyocardium. The knockout myocardium resulted in a different angle transition pattern, where fibers show a quicker transition from left-handed to circumferential before the midwall, closer to the subepicardium. The helix angles of cMyBP-C$^{-/-}$ hearts range from an average of -39° on the subepicardium to 48° on the subendocardium. The fibers approach circumferential 0° fibers before reaching the midwall. The fiber angles transition continuously, as with the wild type, but at a faster, more consistent rate. Also note in Figure 4.1.8, helix angle measurements could not be extracted for fibers lying from the midwall to the subendocardium. Here, unorganized fiber disorder dominates the myocardium and results in several different fiber orientations as previously shown by average tract lengths. In addition, in the inner left ventricular wall, the number of fiber tracts running through the spherical region of interest decreases drastically compared to the wild type myocardium.

On the subepicardial surface, the wild type heart shows negative yellow-green tracts, while the cMyBP-C$^{-/-}$ heart shows green-light blue circumferential helices (Fig. 4.1.9). On the subendocardial surface, the wild type remains strongly coherent with positive pink fibers.

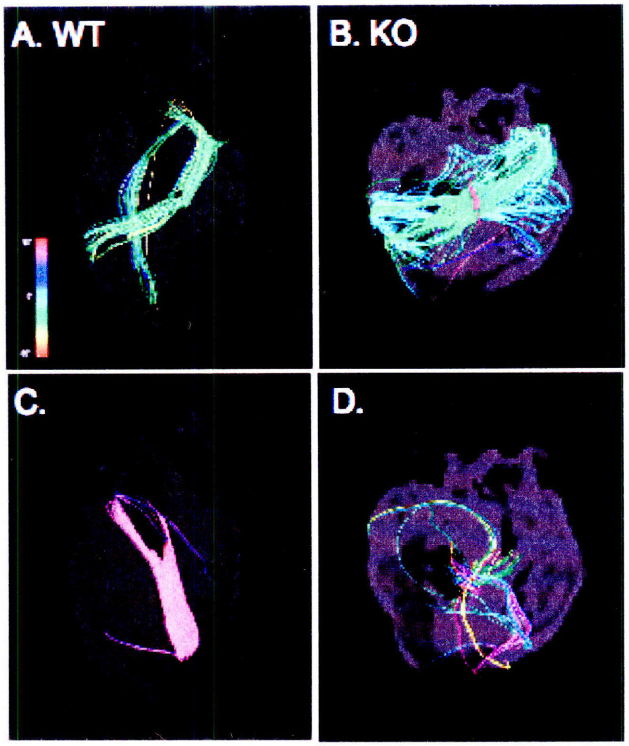

Figure 4.1.9. Isolated subepicardial and subendocardial fibers of wild type (WT) and knockout (KO) hearts shown from the 2 chamber, left ventricle view. A ROI sphere was used to isolate fibers from DSI projections. (A) and (B) display fibers on the subepicardial surface. (C) and (D) display fibers on the subendocardial surface. While (A) and (B) both display coherent tracts, fibers on the subendocardium differ. The WT (C) fibers remain strongly coherent, and the KO (D) fibers are few and disorganized. These images are taken from the same WT and KO hearts as in Figure 4.1.7.

The knockout tracts, on the other hand, are few and appear randomly oriented. In Figure 4.1.9D, the fibers display helix angles at the two opposite ends of the color spectrum, ranging from -62° (yellow) to 66° (pink). From DSI projections and the lack of helix angle measurements, the disorganization of tracts dominates throughout the midwall and subendocardium. Although all the knockouts decrease in fiber tract length and lack a definite helix angle at this location, the manner in which the fibers become disordered appears unique to each heart (Fig. 4.1.10).

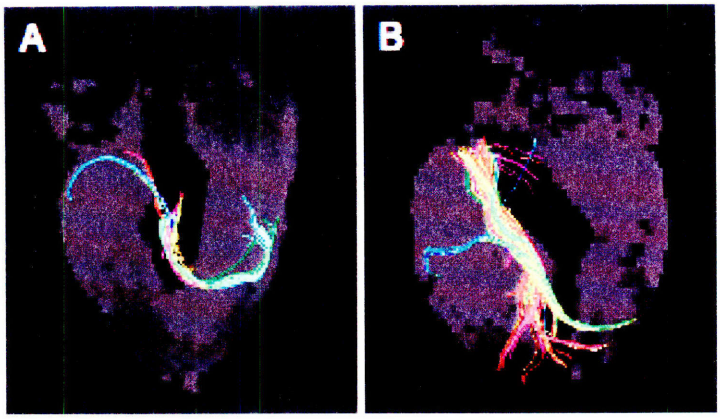

Figure 4.1.10. DSI projection of fibers lying on the subendocardial surface of two knockout mouse hearts different from that pictured in Figure 4.1.9B and 4.1.9D. The myocardium of both knockout hearts (A) and (B) are disrupted from the midwall to subendocardium, but take on different patterns of disorder.

4.3 Effect of cMyBP-C gene deletion on myoarchitecture and mechanics

DSI tractography of wild type mouse hearts displayed a gradual variation in helix angle from subepicardium to subendocardium. The resulting fiber tracts from TPM and DSI support the organization of helical fibers from prior studies. TPM, unlike histology, which depicts 2D subendocardial or subepicardial fibers in a plane, is able to display the fiber patterns in a 3D reconstruction of the myocardium. TPM is able to depict the mesoscopic fiber structure of cardiac tissue from images of 3D microscopic sections. TPM of the knockout myocardium confirms the fiber pattern resulting from DSI. From extraction of helix angles from both TPM and DSI, the evolution of helical fiber patterns matches results previously shown by Streeter [4], but with a smaller range of angles. The transition of helix angles from subepicardium to subendocardium remains fairly consistent at various locations on the left ventricular wall, depending on the relative wall thickness. The formation of spiraling helical

sheets is important to the development and exertion of contractile force throughout the myocardium.

The architectural changes caused by the absence of cMyBP-C were not as apparent as the fiber void seen in infracted hearts. The knockout hearts posses the same general features as the wild type hearts (Fig. 4.1.5 and Fig. 4.1.1). By examining average fiber tract length on the left ventricular wall as a function of depth, it was found that the knockout myocardium reached a maximum length in the subepicardium, while the wild type reached a maximum at the midwall. Beginning around the midwall, the knockout myocardium displayed shortened fibers and inconsistent fiber helix angles. The lack of fiber order and paucity of fiber tracts fibers from the midwall to subendocardium indicated that there is weaker diffusion in the inner half of the ventricular wall. The diffusion in this instance could also be consistent with more isotropic conditions than in the normal myocardium. Accordingly, the resulting fiber tracts lack the intervoxel coherence that exists in normal myocardium.

The myofiber disorder found in the inner half of the ventricular wall may result from growth process of the heart. The development of the epicardium, myocardium, and endocardium occurs at different stages of cardiac embryogenesis. Contraction begins when the primitive tubular heart is formed, and as the myocardium develops, blood is directed unidirectionally [58]. The heart tube consists of a concentric endocardial and myocardial tube separated by "cardiac jelly". The tube then begins a looping process, which initiates the formation of the four chambers [59]. After the heart tube is formed and looped, endocardial cells undergo an "epithelial-to-mesenchymal transformation (EMT)" where they continue to differentiate into the subendocardium [60]. Simultaneously, an epithelial proepicardium begins to form at the

surface of the myocardium. Unlike endocardial cells, these epicardial cells are derived from a non-precardiac origin [60]. As this outer cell layer is formed, epicardial cells begin to generate the subepicardium through its own EMT, connecting the myocardium to the epicardium.

Two different populations of cells are therefore formed at each side of the myocardium. The different origins of the inner and outer myocardium give reason for myofiber disorder in only one of these regions (subendocardium) of the cMyCP-C$^{-/-}$ heart. Both subendocardium and subepicardium are both important to the development of the heart. However, because the maturation of the subendocardium occurs earlier on, it is possible that the absence of cMyBP-C accordingly affects subendocardial myofiber arrangement beginning at embryonic stages. The lack of helices here alters the transmural progression of helices in the subepicardium. In knockout myocardium, the complete transition from negative to positive angles, as observed in the wild type hearts, develops only from subepicardium to midmyocardium.

The lack or organization from the midwall to the subendocardium suggests that the inner ventricular wall of the mutant heart is less developed than that of the wild type, and in comparison, may induce less contractile force. Within the knockout myocardium, the subepicardium appears more developed than the subendocardium in terms of intervoxel coherence and helicity. This disorder of myofibers may play a role in the delayed increase in force, thereby leading to depressed systolic and diastolic function. Preliminary studies have shown that cMyBP-C$^{-/-}$ hearts have a shortened contraction time consistent with depressed systolic ejection [61,62], and furthermore, reach 77% of maximum peak elastance at the onset of ejection, whereas wild type hearts only reached 42% of its maximum [63]. The faster transition

from negative to positive helix angles in the subepicardium of the knockout myocardium may enhance the extent of initial elastance by means of faster contractile force activation. The quicker onset of elastance and lack of helical fiber development from the midwall to the subendocardium also supports findings of shorter overall contractile time in the cardiac cycle. With less helically aligned fibers to stretch during contraction, the cMyBP-$C^{-/-}$ muscle tissue would also relax earlier than the normal myocardium.

The disruption of the fiber helicity alters the normal contractile twisting of the cardiac tissue. During normal contractile shearing, fibers in the subepicardium and subendocardium become more longitudinal [13]. The overall torsional movement of the heart, however, follows the left-handed helices of the subepicardium[3], and thus some believe the subepicardium to initiate contraction. In the knockout, the myofibers transition more rapidly and linearly from left- to right-handed helices within the subepicardium. The faster increase of force at the onset of contraction is consistent with the quick progression of fiber helix angles restricted from the subepicardium to the midmyocardium.

On the other hand, wall thickening during systole and thinning during diastole occurs at a much greater degree in the subendocardium [11], and therefore, plays a more significant role in the overall cardiac mechanics. According to Davis and Streeter, the angle of rotation in the subendocardium is greater than that in the subepicardial surface [3, 13], and so subendocardial fibers reach larger angles (in magnitude). Also, higher pressure has been measured in the subendocardium during systole [55]. If the endocardium plays a greater role in during the development of contractile force, which proceeds by means of twisting helical fibers, the

lack of coherent fibers in the knockout subendocardium would hinder systolic function and lead to a shorter duration of force.

In relation to molecular cross-bridge cycling, thin filament activation and contraction is mostly facilitated by strongly bound cross-bridges[28]. In theory, the absence of cMyBP-C$^{-/-}$ increases the amount of myosin-actin interactions. However, a single cMyBP-C protein affects only a small number of cross-bridges. Models with phosphorylated cMyBP-C also observed a decrease in flexibility of cross-bridges [26, 30]. The combination of these factors with myofiber disorganization in the midmyocardium to subendocardium may decrease the amount of cross-bridge activity. The existing cross-bridges would unbind more quickly, preventing further activation of the cross-bridge cycle, and lead to a shorter contraction and longer relaxation time.

Chapter 5

Conclusion

Cardiac muscle fiber alignment within the left ventricular wall is described as a set of sheets consisting of helical fibers that transition smoothly from negative angles in the subepicardium to zero degrees in the midmyocardium to positive angles in the subendocardium. The presence of shared fibers between the left and right ventricles indicates the coupling of mechanical and electrical activation of the two ventricles. Normal myoarchitecture of spiraling helices throughout the ventricular walls supports the contractile twisting and activation sequence of the heart.

Infarction causes injury to cardiac tissue, thinning of ventricular walls, and compensatory hypertrophy, leading to abnormal mechanics. Post infarction, the myocardium enters stages of remodeling where the injured tissue is largely replaced by collagen scar tissue. The myoarchitecture is characterized by a fiber void in the infarct zone and a growth of a fiber mesh-like structure penetrating the border zone. The growth of both subendocardial and subepicardial fibers suggests the importance of both to normal cardiac functioning. This act of remodeling provides tensile strength to the infarct zone and permits partial recovery of mechanical function.

Further studies are needed to understand the formation of this mesh and its mechanical influences. DSI tractography on hearts at various time stages post infarction can be used to further investigate the sequence of fiber formation in the infarct zone. The initial formation of subepicardial or subendocardial fibers will dictate the how the heart compensates mechanically. The continuing development of DSI will allow non-invasive imaging of other species, including humans, to determine whether a similar myofiber pattern is formed during remodeling.

In contrast, the hearts obtained from the cMyBP-C knockouts displayed significant myoarchitectural disarray, characterized by a loss of voxel-to-voxel orientational coherence for those fibers principally located from the mid-myocardium to subendocardium resulting in a change in the transmural progression of helix angles in the subepicardium. The alterations in fiber pattern causes changes in force development, causing a quicker onset of contraction and a shorter period of ejection [61, 62]. The loss of the normal fiber helicity in cMyBP-C$^{-/-}$ hearts leads to abnormal force development during contraction and relaxation. These results provide evidence of an association between myofilament expression and cardiac fiber alignment, and suggest that variations in torsional rotation may constitute a mechanism for pump failure in the setting of hypertrophic cardiomyopathy.

Future studies using DSI to explore the development of a knockout heart at different stages of growth would be advantageous to reveal the progression of abnormal fiber alignment caused by the lack of cMyBP-C. It would provide further insight on the impact of cMyBP-C on cross-bridge cycling and myosin-actin activation. Incorporation of DSI findings into a

simulation model of cardiac muscle contraction based on molecular interactions would fill gaps in the understanding of cardiac pathology caused by the lack of cMyBP-C.

The basis of understanding heart failure lies in the way in which molecular changes in myocyte contractility affect the local deformation and 3D alignment of myocytes. DSI and TPM are able to extrapolate tissue-scale fiber organization from microscopic diffusion directions and cell morphology. Such imaging methods prompt the understanding of mechanical and electrical activation of myocytes and the coupling of function among fiber layers. The use of DSI and TPM to reveal the 3D macroscopic myoarchitecture of normal, infarcted, and cMyBP-$C^{-/-}$ hearts provides such a link, and sets the stage for the development of new therapies designed to induce normal mechanics. It will become increasingly important to study the clinical effects of tissue engineering solutions aimed to decrease the risk of heart failure.

Bibliography

1. A.D.A.M, I. Circulation of blood through the heart. U.S. National Library of Medicine-National Institute of Health. Medline Plus. http://www.nlm.nih.gov/medlineplus/ency/imagepages/19387.htm (2006).

2. Gray, H. Anatomy of the Human Body. V. Angiology – The Heart. 20th Ed. Online Version - http://www.bartleby.com/107/. (1918).

3. Davis, J. S., Hassanzadeh, S., Winitsky, S., Lin, H., Satorius, C., Vemuri, R., Aletras, A. H., Wen, H. & Epstein, N.D. The overall pattern of cardiac contraction depends on a spatial gradient of myosin regulatory light chain phosphorylation. *Cell.* **107**, 631-641.

4. Streeter, D. D., Spotnitz, H. M., Patel, D. P. & Ross, J. Fiber Orientation in the Canine Left Ventricle during Diastole and Systole. *Circ. Res.* **24**, 339-347 (1969).

5. Tseng, W. Y., Reese, T. G., Weisskoff, R. M., Brady, T. J. & Wedeen, V. J. Myocardial fiber shortening in humans: initial results of MR imaging. *Radiology.* **216**, 128-139 (2000).

6. Greenbaum, R. A., Ho, S. Y., Gibson, D. G., Becker, A. E. & Anderson, R. H. Left ventricular fiber architecture in man. *British Heart Journal.* **45**, 248-263 (1981).

7. Streeter, D. D. & Hanna, W. T. Engineering Mechanics for Successive States in Canine Left Ventricular: I. Cavity and Wall Geometry. *Circ. Res.* **33**, 639-655 (1973).

8. LeGrice, I. J., Takayama, Y. & Covell, J. W. Transverse shear along myocardial cleavage planes provides a mechanism for normal systolic wall thickening. *Circ. Res.* **77**, 182-193 (1995).

9. Dou, J., Tseng, W. I., Reese, T. G. & Wedeen, V. J. Combined diffusion and strain MRI reveals structure and function of human myocardial laminar sheets in vivo. *Magnetic Resonance Medicine.* **50**, 107-113 (2003).

10. Torrent-Guasp, F., Kocica, M. J., Corno, A. F., Komeda, M., Carreras-Costa, F., Flotats, A., Cosin-Aguillar, J. & Wen, H. Towards new understanding of the heart structure and function. *European Journal of Cardio-Thoracic Surgery.* **27**, 191-201 (2005).

11. Sabbah, H. N., Marzilli, M. & Stein, P. D. The relative role of subendocardium and subepicardium in left ventricular mechanics. *Am. J. Physiol.* **240(6)**, H920-H926 (1981).

12. Hunter, P. J., Pullan, A. J., & Smaill, B. H. Modeling total heart function. *Annua. Rev. Biomed. Eng.* **5**, 124-177 (2003).

13. Streeter, D. D. & Hanna, W. T. Engineering Mechanics for Successive States in Canine Left Ventricular: II. Fiber Angle and Sarcomere Length. *Circ. Res.* **33**, 656-664 (1973).

14. Dou, J., Reese, T. G., Tseng, W. Y. I. & Wedeen, V. J. Cardiac diffusion MRI with-out motion effects. *Magnetic Resonance Medicine.* **48**, 105-114 (2002).

15. World Health Organization. The world health report 2004 - Changing history. **ISBN 92-4-156265-X**, 120-124 (2004).

16. Wickline, S. A., Verdonk, E. D., Wong, A. K., Shepard, R. K. & Miller, J. G. Structural remodeling of humans myocardial tissue after infarction. *Circulation.* **85**, 259-268 (1992).

17. Pfeffer, M. A. & Braunwald, E. Ventricular remodeling after myocardial infarction. Experimental observations and clinical implications. *Circulation.* **81**, 1161-1172 (1990).

18. Cohn, J. N., Ferrari, R., Sharpe, N. & on Behalf of an International Forum on Cardiac Remodeling. Cardiac remodeling - concepts and clinical implications: a consensus paper from an international forum on cardiac remodeling. *Journal of the American College of Cardiology.* **35**, 569-582 (2000).

19. Cleutjens, J. P. M., Blankesteijn, W. M. & Daemen, M. J. A. P. The infarcted myocardium: Simply dead tissue, or a lively target for therapeutic interventions. *Cardiovasc. Res.* **44**, 232-241 (1999).

20. Helm, P. A., Younes, L., Beg, M. F., Ennis, D.B., Leclercq, C., Faris, O. P., McVeigh, E., Kass, D., Miller, M. L. & Winslow, R. L. Evidence of structural remodeling in the dyssynchronous failing heart. *Circ. Res.* **98**, 125-132 (2006).

21. Wu, M., Tseng, W. I., Su, M. M., Liu, C., Chiou, K., Wedeen, V J., Reese, T. G. & Yang, C. Diffusion tensor magnetic resonance imaging mapping the fiber architecture remodeling in human myocardium after infarction: correlation with viability and wall motion. *Circulation.* **114**, 1036-1045 (2006).

22. Chen, J., Song, S., Liu, W., McLean, M. & Allen, J. S. Remodeling of cardiac fiber structure after infarction in rats quantified with diffusion tensor MRI. *Am. J. Physiol. Heart Circ. Physiol.* **285**, H946-H954 (2003).

23. Flashman, E., Redwood, C., Moolman-Smook, J. & Watkins, H. Cardiac Myosin Binding Protein C. *Circ. Res.* **94**, 1279-1289 (2004).

24. Spirito, P., Seidman, C. E., McKenna, W. J. & Maron, B. J. The management of hypertrophic cardiomyopathy. *New England Journal of Medicine.* **336**, 775-785 (1997).

25. Calaghan, S. C., Trinick, J., Knight, P. J. & White, E. A role for C-protein in the regulation of contraction and intracellular Ca^{2+} in intact rat ventricular myocytes. *J. Physiol. (Lond.).* **528(1)**, 151-156 (2000).

26. Winegrad, S. Cardiac Myosin Binding Protein C. *Circ. Res.* **84**, 1117-1126 (1999).

27. Pohlmann, L., Kröger, I., Vignier, N., Schlossarek, S., Krämer, E., Coirault, C., Sultan, K.R. El-Armouche, A., Windgrad, S., Eschenhagen, T. & Carrier, L. Cardiac myosin-binding protein C is required for complete relaxation in intact myocytes. *Circ. Res.* **101**, 928-938 (2007).

28. Stelzer, J. E., Fitzsimons, D. P., & Moss, R. L. Ablation of myosin-binding protein-C accelerates force development in mouse myocardium. *Biophys. J.* **90(11)**, 4119-4127 (2006).

29. Harris, S. P., Bartley, C. R., Hacker, T. A., McDonald, K. S., Douglas, P. S., Greaser, M.L. Powers, P. A. & Moss, R. L. Hypertrophic cardiomyopathy in cardiac myosin binding protein-C knockout mice. *Circ. Res.* **90**, 594-601 (2002).

30. Colson, B. A., Bekyarova, R., Fitzsimons, D. P., Irving, T. C. & Moss, R. L. Radial displacement of myosin cross-bridges in mouse myocardium due to ablation of myosin binding protein-C. *Journal of Molecular Biology.* **367**, 36-41 (2007).

31. Lin, C. P., Wedeen, V. J., Chen, J. H., Yao, C. & Tseng, W. Y. Validation of diffusion spectrum magnetic resonance imaging with manganese-enhanced rat optic tracts and ex vivo phantoms. *Neuroimage.* **19**, 482-495 (2003).

32. Tuch, D. S. Diffusion MRI of Complex Tissue Structure. PhD thesis, Massachusetts Institute of Technology. (2002).

33. Wedeen, V. J., Reese, T. G., Tuch, D. S., Wiegell, M. R., Dou, J. G., Weissoff, R. M., & Chessler, D. Mapping fiber orientation spectra in cerebral white matter with Fourier-transform diffusion MRI. *Presented at the 8th Annual meeting of the International Society of Magnetic Resonance Medicine.* Devner, Colorado. (2000).

34. Gilbert, R. J., Magnusson, L. H., Napadow, V. J. & Benner, T. Mapping complex myoarchitecture in the bovine tongue with diffusion-spectrum magnetic resonance imaging. *Biophys. J.* **91**, 1014-1022 (2006).

35. Gilbert, R. J. & Napadow, V. J. Three-dimensional muscular architecture of the human tongue determined in vivo with diffusion tensor magnetic resonance imaging. *Dysphagia.* **20**, 1-7 (2005).

36. Gaige, T. A., Kwan, H. S., Benner, T., Wang, R., Dai, G., Wedeen, V. J., So, P. T. & Gilbert, R. J. Deriving mesoscale myoarchitecture of the mouse tongue with

multiphoton microscopy and diffusion spectrum magnetic resonance imaging. *Journal of Biomedical Optics.* ((In press)).

37. Gilbert, R. J., Wedeen, V. J., Magnusson, L. H., Benner, T., Wang, R., Dai, G., Napadow, V. J. & Roche, K. K. Three-dimensional myoarchitecture of the bovine tongue demonstrated by diffusion spectrum magnetic resonance imaging with tractography. *Anat Rec A Discov Mol Cell Evol Biol.* **288**, 1173-1182 (2006).

38. Basser, P. J. Fiber-tractography via diffusion tensor MRI (DT-MRI). *Presented at the 6th Annual Meeting of the International Society of Magnetic Resonance ISMRM.* Sydney, Australia. (1998).

39. Chen, J., Liu, W., Zhang, H., Lacy, L., & Yang, X. Regional quantification with diffusion tensor MRI. *Am. J. Physiol. Heart Circ. Physiol.* **289**, H1898-907 (2005).

40. Wedeen, V. J., Hagmann, P., Tseng, W. Y., Reese, T. G. & Weisskoff, R. M. Mapping complex tissue architecture with diffusion spectrum magnetic resonance imaging. *Magnetic Resonance Medicine.* **54**, 1377-1386 (2005).

41. Gaige, T. A. Complex muscle architecture described with diffusion weighted MRI. MS thesis, Massachusetts Institute of Technology. (2007).

42. Brown, M. A. & Semelka, R. C. *MRI Basic Principles and Applications.* (John Wiley and Sons, Inc., New Jersey, 2003).

43. Peyrat, J. M., Sermesant, M., Pennec, X., Delingette, H., Xu, C., McVeigh, E. R. & Ayache, N .A. A computational framework for the statistical analysis of cardiac diffusion tensors: application to a small database of canine hearts. *IEEE Transactions on Medical Imaging.* **26**, 1500-1514 (2007).

44. Tseng, W. Y., Wedeen, V. J., Reese, T. G., Smith, R. N. & Halpern, E. F. Diffusion tensor MRI of myocardial fibers and sheets: correspondence with visible cut-face texture. *Journal of Magnetic Resonance Imaging.* **17**, 31-42 (2003).

45. Le Bihan, D. Looking into the functional architecture of the brain with diffusion MRI. *Nature Reviews Neuroscience.* **4**, 469-480 (2003).

46. Hagmann, P., Johnasson, L., Maeder, P., Thiran, J. P., Wedeen, V. J. & Meuli, R. Understanding diffusion MR imaging techniques: from scalar diffusion-weighted imaging to diffusion tensor imaging and beyond. *Radiographics.* **26**, S205-S223 (2006).

47. Garrido, L., Wedeen, V. J., Kwong, K. K., Spencer, U. M. & Kantor, H. L. Anisotropy of water diffusion in the myocardium of the rat. *Circ. Res.* **8**, 554-560 (1994).

48. Bloch, F. Nuclear induction. *Physical review.* **70**, 460-474 (1946).

49. Torrey, H. C. Bloch Equations with Diffusion Terms. *Phys. Rev.* **104**, 563-565 (1956).

50. Stejskal, E. O. & Tanner, J. E. Spin diffusion measurements - spin echoes in presence of a time-dependent field gradient. *J. Chem. Phys.* **42**, 288-292 (1965).

51. Stejskal, E. O. & Tanner, J. E. Use of spin echoes in a pulsed magnetic field gradient to study anisotropic restricted diffusion and flow. *J. Chem. Phys.* **43**, 3597-3603 (1965).

52. Yu, B., Hean Kim, K., So, P. T., Blankschtein, D. & Langer, R. Topographic heterogeneity in transdermal transport revealed by high-speed two-photon microscopy: determination of representative skin sample sizes. *Journal of Investigatvive Dermatology.* **118**, 1085-1088 (2002).

53. Ragan, T., Sylvan, J. D., Kim, K. H., Huang, H., Bahlmann, K., Lee, R. T. & So, P. T. High-resolution whole organ imaging using two-photon tissue cytometry. *Journal of Biomedical Optics.* **12**, 14015 (2007).

54. Kim, K. H., Buehler, C. & So, P. T. C. High-speed, two-photon scanning microscope. *Appl. Opt.* **38**, 6004-6009 (1999).

55. Yin, F. C. Ventricular wall stress. *Circ. Res.* **49**, 829-842 (1981).

56. Christman, K. L. & Lee, R. J. Biomaterials for treatment of myocardial infarction. *Journal of the American College of Cardiology.* **48**, 907-913 (2006).

57. Hooks, D. A., Trew, M. L., Caldwell, B. J., Sands, G. B., LeGrice, I. J. & Smaill, B. H. Laminar arrangement of ventricular myocytes influences electrical behavior of the heart. *Circ. Res.* **101**, 103-112 (2007).

58. Smith, T. K. & Bader, D. M. Signals from both sides: Control of cardiac development by the endocardium and epicardium. *Cell & Developmental Biology.* **18**, 84-89 (2007).

59. Eisenberg, L. M. & Markwald, R. R. Cellular recruitment and the development of the myocardium. *Developmental Biology.* **274**, 225-232 (2004).

60. Wessels, A. & Perez-Pomares, J. M. The Epicardium and Epicardially Derived Cells (EPDCs) as Cardiac Stem Cells. *The Anatomical Record Part A.* **276A**, 43-57 (2004).

61. Korte, R. S., McDonald, K. S., Harris, S. P. & Moss, R. L. Load shortening, power output, and rate of force redevelopment are increased with knockout of cardiac myosin binding protein-C. *Circ. Res.* **93**, 752-758 (2003).

62. Stelzer, J. E., Dunning, S. B. & Moss, R. L. Ablation of cardiac myosin-binding protein-C accelerates stretch activation in murin skinned myocardium. *Circ. Res.* **98**, 1212-1218 (2006).

63. Palmer, B. M., Georgakopoulos, D., Janssen, P. M., Want, Y., Alpert, N. R., Belardi, D.F., Harris, S. P., Moss, R. L., Burgon, P. G., Seidman, C. E., Maughan, D. W. & Kass, D. A. Role of cardiac myosin binding protein C in sustaining left ventricular systolic stiffening. *Circ. Res.* **94**, 1249-1255 (2004).